# Coherent Structures in the Boundary and Cloud Layers: Role of Updrafts, Subsiding Shells, and Environmental Subsidence

Seung-Bu Park, Pierre Gentine, Kai Schneider, Marie Farge

# Coherent Structures in the Boundary and Cloud Layers: Role of Updrafts, Subsiding Shells, and Environmental Subsidence

SEUNG-BU PARK AND PIERRE GENTINE

*Department of Earth and Environmental Engineering, Earth Institute, Columbia University, New York, New York*

KAI SCHNEIDER

*M2P2-CNRS, Aix-Marseille Université, Marseille, France*

MARIE FARGE

*LMD-IPSL-CNRS, Ecole Normale Supérieure, Paris, France*

(Manuscript received 14 August 2015, in final form 3 February 2016)

ABSTRACT

Coherent structures, such as updrafts, downdrafts/shells, and environmental subsidence in the boundary and cloud layers of shallow convection, are investigated using a new classification method. Using large-eddy simulation data, the new method first filters out background turbulence and small-scale gravity waves from the coherent part of the flow, composed of turbulent coherent structures and large-scale transporting gravity waves. Then the algorithm divides this coherent flow into ''updrafts,'' ''downdrafts/shells,'' ''subsidence,'' ''ascendance,'' and four other flow structures using an octant analysis. The novel method can systematically track structures from the cloud-free boundary layer to the cloud layer, thus allowing systematic analysis of the fate of updrafts and downdrafts. The frequency and contribution of the coherent structures to the vertical mass flux and transport of heat and moisture can then be investigated for the first time. Updrafts, subsidence, and downdrafts/subsiding shells—to a lesser extent—are shown to be the most frequent and dominant contributors to the vertical transport of heat and moisture in the boundary layer. Contrary to previous perspective, environmental subsidence transport is shown to be weak in the cloud layer. Instead, downdrafts/shells are the main downward transport contributors, especially in the trade inversion layer. The newly developed method in this study can be used to better evaluate the entrainment and detrainment of individual—or an ensemble of—coherent structures from the unsaturated boundary layer to the cloud layer.

## 1. Introduction

Clouds are one of the biggest uncertainties in climate prediction using general circulation models (GCMs), and these uncertainties are partly attributed to the incomplete parameterization of convection (Bony et al. 2006). Many efforts have been made to improve convective parameterizations in GCMs, and continuous progress has been made by considering a unified representation of turbulence in the boundary layer and cloud layer (Soares et al. 2004; Siebesma et al. 2007; Rio and Hourdin 2008; Neggers 2009; Gentine et al. 2013a,b; Sušelj et al. 2013; D'Andrea et al. 2014) and by refining plume characteristics (e.g., lateral entrainment) (Kim et al. 2012). Despite the progress, convective parameterization remains one of the main challenges of current GCMs, and it requires more systematic studies on the interaction (i.e., entrainment and detrainment) between convective structures (defined as organized turbulent motion; e.g., updrafts and downdrafts) and the environment (de Rooy et al. 2013).

The basic coherent structures in moist convection have been studied for a long time (Bretherton 1987; Bretherton and Smolarkiewicz 1989; Heus and Jonker 2008; Sherwood et al. 2013). Bretherton (1987) showed that heating from below and stable stratification between parallel plates induce internal circulation similar

*Corresponding author address*: Seung-Bu Park, Department of Earth and Environmental Engineering, Columbia University, 500 West 120th Street, 842H S. W. Mudd, New York, NY 10027.
E-mail: sp3338@columbia.edu

DOI: 10.1175/JAS-D-15-0240.1

to Hill's vortex (Hill 1894) with vertical motion in the condensed region of updrafts and descending motion around it. Similar internal circulation appears in updrafts in shallow convection (Heus and Jonker 2008) and deep convection (Sherwood et al. 2013; Glenn and Krueger 2014). The downward branch of the internal circulation is typically called the ''subsiding shell,'' and this shell is known to change the properties of entrained and detrained air, affecting calculations of the rate of entrainment and detrainment (exchange of air) between the updraft and the environment (Heus and Jonker 2008; Abma et al. 2013). However, most entrainment and detrainment parameterizations are based on bulk mass flux approaches, which assume a top-hat distribution of velocity and scalars with one uniform value given to the updraft and one uniform value given to the environment (Gregory 2001; de Rooy et al. 2013). By definition, those approaches do not consider subsiding shells or other surrounding vertical motions (Tiedtke 1989; Bechtold et al. 2008) and could be misleading (Heus and Jonker 2008; Abma et al. 2013). For instance, Dawe and Austin (2011) confirmed that the larger entrainment and detrainment found in direct measurements of entrainment (Romps 2010) could be related to the presence of subsiding shells.

Despite their achievements, previous studies have limitations in their investigation of convective structures. Indeed, the definition of convective structures is typically unclear or case specific; the complexity of turbulent flow is often overlooked; and, except for very few studies, (Couvreux et al. 2010; Rio et al. 2010) the entrainment and detrainment analysis can only be performed in the cloudy state when coherent structures are assumed to be condensed and in the upward part of the flow. Nonetheless, coherent structures can be complex and can exhibit both upward and downward motions [such as Hill's vortices (Bretherton 1987; Bretherton and Smolarkiewicz 1989; Heus and Jonker 2008; Sherwood et al. 2013; Glenn and Krueger 2014)]. As a result, there is no consensus yet on defining convective coherent structures. The widely used ''updraft cores,'' defined as cloudy updrafts that are buoyant or whose vertical velocity is faster than a threshold value, is typically used to illustrate the central part of moist convection, yet, like most methods, it relies on a threshold.

Background—incoherent, mostly random—turbulence and small-scale gravity waves, which are omnipresent in the boundary and cloud layers, make it even more difficult to clarify boundaries between the aggregated convective structures and the environment (Pauluis and Mrowiec 2013; Mrowiec et al. 2015). In addition, most of the previously used methods cannot detect convective structures evolving from the boundary layer to the cloud layer because they rely on a threshold for the condensed moisture, except for the method in Couvreux et al. (2010) and Rio et al. (2010), which is based on an additional scalar threshold. To overcome these limitations, a new method should be introduced to systematically classify ''coherent'' convective structures, including updraft, subsiding shell, environmental subsidence, and others.

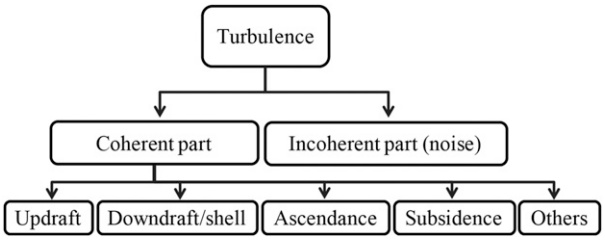


FIG. 1. Schematic of classified coherent flow patterns.

''Coherent structures'' are widely used to represent a distinct and dominant turbulent flow structure in engineering and geoscience communities (Robinson 1991; Haller and Yuan 2000; Farge et al. 2001, 2006; Finnigan et al. 2009; Beron-Vera et al. 2015; Richter and Sullivan 2014). In this study, we call coherent structures the part of the flow that explains most of the vertical transport in the boundary and cloud layers using a coherent structure extraction method developed for the study of diverse turbulent flows (Farge et al. 2001, 2006; Schneider et al. 2005; Bos et al. 2008; Kadoch et al. 2011; Wilczek et al. 2012; Okamoto et al. 2011a). We note that this method can also extract larger-scale (transporting) gravity waves (Kershaw 1995). The method is developed to determine an objective and universal tracking of coherent structures in the unsaturated boundary layer and track their evolution through the cloud layer.

The main idea behind the incoherent versus coherent flow decomposition dates back to Tollmien and Prandtl, who suggested that ''turbulent fluctuations might consist of two components, a diffusive and a nondiffusive component .... Considerable masses of fluid move as more or less coherent units. The process cannot be smoothed by averaging over a small volume because it is not possible to choose dimensions small compared with the boundary layer thickness and at the same time large compared with a single fluid element'' (Dryden 1948, pp. 35, 38). As illustrated in Fig. 1, our new method first filters this incoherent (random) part of the flow from the coherent (organized) part of the flow computed by a large-eddy simulation (LES) model. The incoherent part of the flow increases with the LES resolution (Farge et al. 2001) as the subgrid-scale high-pass filtering becomes smaller and more of the high-wavelength flow is resolved. Indeed the subgrid-scale model effectively filters

out the high-frequency part of the flow. On the other hand in cloud-resolving models, the horizontal grid sizes of which are typically larger than 500 m, the flow exhibits few turbulent fluctuations so that coherent versus incoherent filtering is not needed (see later discussion). In our high-resolution LES data, it is essential to first filter out the coherent part of the flow to avoid background turbulent ''noise'' pollution of the structure decomposition (see section 2b). The filtered coherent part is then divided into coherent structures, such as updraft, downdraft/shell, ascendance, and subsidence, and their contribution to the transport is analyzed.

The manuscript is divided as follows. The filtering and classifying methods and simulation setup are described in section 2. The coherent flow structures are analyzed in section 3. A summary and conclusions are given in section 4.

## 2. Methodology

### a. Large-eddy simulation

The University of California, Los Angeles, large-eddy simulation (UCLA-LES) model (Stevens et al. 1999, 2005; Stevens and Seifert 2008) is used to simulate shallow cumulus convection. The UCLA-LES model solves the implicitly filtered prognostic equations of velocity components, liquid water potential temperature $\theta_l$, and total water mixing ratio $q_{\text{tot}}$. In addition, we added two passive scalars $s_1$ and $s_2$ for coherent structure decomposition (see the details in section 2c). Passive scalars are useful for updraft and downdraft tracking in both the boundary and cloud layers (Couvreux et al. 2010; Rio et al. 2010). The prognostic equations on a three-dimensional grid are integrated using the third-order Runge–Kutta scheme. The Smagorinsky model is used to parameterize subgrid-scale (SGS) fluxes of momentum, heat, and other scalars. Both the eddy Prandtl number and eddy Schmidt number are 1/3. Only the reversible conversion between water vapor and liquid water is considered in this nonprecipitating convection case, and the liquid water mixing ratio is diagnostically calculated using a saturation adjustment scheme. The trade wind cumuli in the Barbados Oceanographic and Meteorological Experiment (BOMEX; Holland and Rasmusson 1973; Siebesma et al. 2003) are simulated using the initial sounding and external forcing described in Siebesma et al. (2003). The grid size in both the $x$ (west–east) and $y$ (south–north) directions is 25 m; the vertical ($z$) grid size $\Delta z$ is 20 m below $z = 2570$ m, and it increases to 54.4 m above that level. The computational domain size is $12.8 \times 12.8 \times \sim 3\,\text{km}^3$ with $512 \times 512 \times 144$ grid points. The trade wind cumuli are simulated for 6 h, and 1-min-interval data are stored and analyzed in the last 30 min of the simulation, when steady state is reached.

Shallow cumuli over land are also simulated using the initial sounding, surface fluxes, and external forcing from observations at the Southern Great Plains (SGP) site on 21 June 1997, part of the Atmospheric Radiation Measurement (ARM) Program (Brown et al. 2002). The computational domain covers $12.8 \times 12.8 \times \sim 5\,\text{km}^3$ with $512 \times 512 \times 180$ grid points. The grid size in the horizontal direction is 25 m, and the vertical grid size increases from 20 to 186.3 m. The cumuli over the ARM SGP site are simulated for 9.5 h, and the fields at three instants (3, 6, and 9 h) are analyzed and presented in section 3d.

### b. Filtering

The coherent vorticity extraction method (CVE; Farge et al. 1999, 2001) is used to filter out incoherent (noise) contribution from coherent flow in the LES data. The method is based on a wavelet decomposition, which has been tested and validated across a wide range of applications and has demonstrated very good decomposition of isotropic turbulent flows (Farge et al. 2001; Kadoch et al. 2011; Okamoto et al. 2011b; Wilczek et al. 2012), turbulent edge plasma (Farge et al. 2006), resistive drift-wave turbulence (Bos et al. 2008), turbulent mixing layers (Schneider et al. 2005), and turbulent boundary layers (Khujadze et al. 2011). The original CVE extracts coherent vorticity by backward transforming wavelet coefficients above a theoretically derived adaptive threshold, which corresponds to denoising. This technique has been applied to both simulation data (Farge et al. 1999, 2003) and turbulence measurements (Farge et al. 2006). First, it decomposes the data into orthogonal wavelets [Coiflet 30 wavelets are used in this study as in Kadoch et al. (2011) and Wilczek et al. (2012)], and then it estimates the level of Gaussian white noise based on an adaptive threshold value. The wavelet coefficients larger than the threshold value $\varepsilon = (2 \ln N\sigma^2)^{1/2}$, where $N$ is the data size and $\sigma^2$ is the noise's variance, are considered to be nonGaussian based on statistical signal theory (Donoho and Johnstone 1994; Farge et al. 2006) and the coherent signal is then computed by backward transforming the nonGaussian wavelet coefficients. A first estimate of the a priori unknown noise variance is the variance of the variable itself (enstrophy for vorticity), and the noise variance is updated by successive iterative processes (Farge et al. 2006) so that the final decomposition of the incoherent flow is independent of the initial threshold selected.

CVE has been applied to two- or three-dimensional data in homogenous turbulence (Farge et al. 1999, 2003,

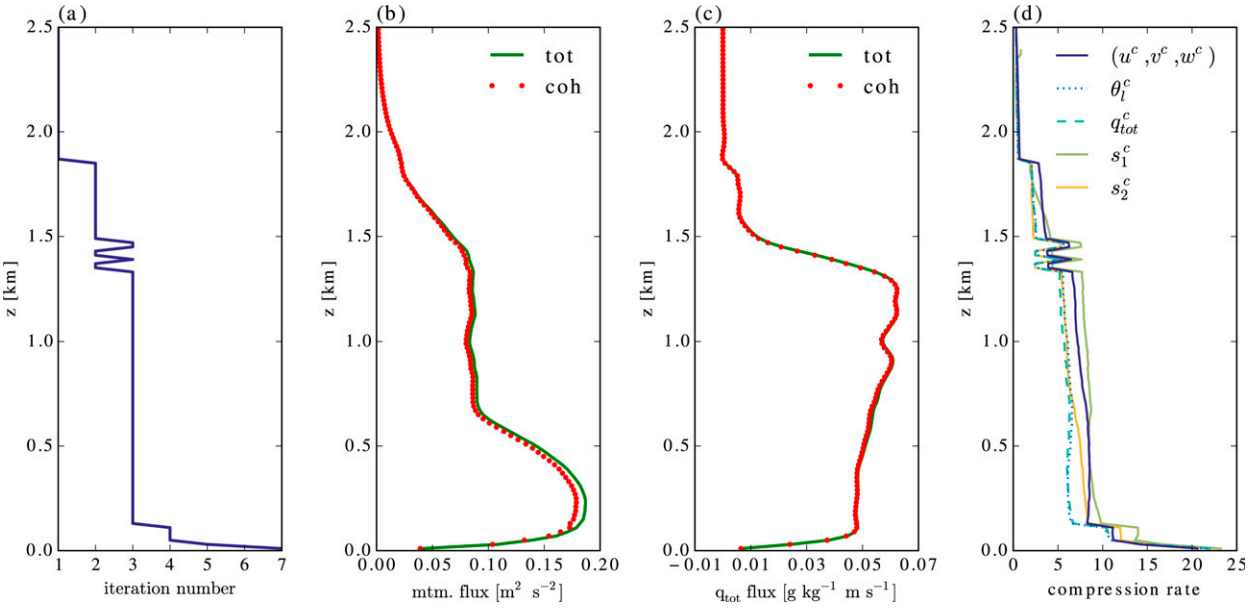


FIG. 2. (a) Iteration number, (b) momentum flux of total (resolved) and coherent parts, (c) moisture flux of total and coherent parts, and (d) compression rate of coherent velocity, coherent liquid water potential temperature, total water mixing ratio, and decaying and nondecaying scalars at $t = 21\,600$ s.

2006). As turbulence in our case is nonhomogeneous in the vertical direction, CVE is applied to two-dimensional horizontal data at 128 $x$–$y$ planes and 30 time instants. It extracts coherent parts of velocity components ($u^c$, $v^c$, and $w^c$) and scalars $\theta_l^c$, $q_{\text{tot}}^c$, $s_1^c$, and $s_2^c$, separately. Here, the superscript $c$ indicates coherent parts. While the noise variance for direct numerical simulation data converges within a few iterations (Okamoto et al. 2007), the noise's variance for LES data decreases with iteration because of the smoothing induced by the subgrid-scale turbulence LES filter. Thus, excessive iterations do not remove the noise but recover the original signal. Unlike previous CVE studies, the optimal iteration number is thus determined by the ratio of coherent to original (total) vertical turbulent momentum fluxes in this study. At each iteration, we check whether the ratio of coherent to total vertical turbulent momentum fluxes is larger than a threshold ratio (assumed to be 95% in this study, but the choice of the threshold is robust and does not alter any of the conclusions). If the ratio is larger than the threshold value, the iteration ends and the denoised data are saved as coherent parts. The iteration number and compression rate (the ratio of coherent to total wavelet coefficients) at the last time step ($t = 21\,600$ s) are presented in section 3e. The compression rate is typically on the order of 7% (Fig. 2). Therefore, even if the coherent part is represented by only 7% of the total number of wavelet coefficients, it contributes to most of the vertical transport and mass flux (Fig. 2). Implications of this efficient compression rate are discussed in the conclusion section.

### c. *Two passive scalars*

Scalars have been used to differentiate between updraft and downdraft convective motions. For instance, entropic analyses have been performed to understand the convective flow characteristics (Pauluis and Mrowiec 2013; Mrowiec et al. 2015). Paluch mixing diagrams have also been used with two scalars, such as liquid water potential temperature and total water mixing ratio (Betts 1985; Kuang and Bretherton 2006; Santanello et al. 2009, 2011). One issue with liquid water potential temperature and total water mixing ratio is that they are highly correlated so that defining the types of coherent structures using these tracers can be misleading. Similarly, entropy in the surface layer has similar values to the values in the cloud layer so that clearly defining source and sink regions is difficult.

To overcome this issue, two near-decorrelated passive scalars are introduced in the LES to better classify coherent flow structures and to illustrate their characteristics. The unitless passive scalar $s_1$ is emitted at the surface, and its kinematic surface flux is set to $1\,\text{m}\,\text{s}^{-1}$. Following Couvreux et al. (2010), $s_1$ is designed to decay with a 30-min time scale at every grid point to avoid oversaturation. Thus, this bottom-up scalar can illustrate uprising convective structures and nearby diffusive structures well. The other unitless passive scalar $s_2$ is set

TABLE 1. Definition of octants based on the signs of $w^{c\prime}$, $s_1^{c\prime}$, and $s_2^{c\prime}$.

| | Octant | | | | | | | |
|---|---|---|---|---|---|---|---|---|
| | 1 | 2 (Updraft) | 3 (Ascendance) | 4 | 5 | 6 (Downdraft/shell) | 7 (Subsidence) | 8 |
| $w^{c\prime}$ | + | + | + | + | − | − | − | − |
| $s_1^{c\prime}$ | + | + | − | − | + | + | − | − |
| $s_2^{c\prime}$ | + | − | + | − | + | − | + | − |

to increase with height initially $[s_{2,0}(z) = 0.001z]$, resembling a stably stratified atmospheric layer. Without turbulent mixing, $s_2$ would thus directly define the height of origin of the coherent structure. Perturbations of $s_2$ from the initial distribution are relaxed toward the initial profile with a 10-min time scale at every grid point to recover the initial state. This short time scale prevents downward accumulation of $s_2$ and the formation of a well-mixed region in the boundary layer, while capturing top-down motions and maintaining a quasi-steady mean state (similar to the initial profile). A sensitivity test is performed on the decay and relaxation time scales for $s_1$ and $s_2$, respectively, and presented in appendix B and shows that the two chosen times scales are appropriate. These two passive scalars with the vertical velocity enable a detailed classification of ascending or descending coherent flow structures.

### d. Octant analysis

The octant analysis, an extended version of the quadrant analysis (Raupach 1981), divides a time series or spatial field of three variables into eight parts based on the signs of flux perturbations of the three variables (Volino and Simon 1994; Gheisi et al. 2006). This type of classification technique is widely used in surface-layer turbulence to decompose the covariance and to investigate their characteristics (Sullivan et al. 1998; Li and Bou-Zeid 2011; Wallace 2016). With the help of CVE and two passive scalars, eight coherent flow structures can be defined based on the signs of $w^{c\prime}$, $s_1^{c\prime}$, and $s_2^{c\prime}$, where prime indicates perturbation from horizontal (slab) average (Table 1). Four of the octants are especially studied here: the "updraft" (octant 2), "ascendance" (octant 3), "downdraft/shell" (octant 6), and "subsidence" (octant 7) (Fig. 1). A combination of positive $s_1^{c\prime}$ and negative $s_2^{c\prime}$ defines the region where air from below has been transported upward, and its upward $w^{c\prime} > 0$ (downward $w^{c\prime} < 0$) velocity component represents the updraft (downdraft/shell). In contrast, a combination of negative $s_1^{c\prime}$ and positive $s_2^{c\prime}$ defines the environment or the region where air from above has been transported, and its upward $w^{c\prime} > 0$ (downward $w^{c\prime} < 0$) velocity component represents the ascendance region (subsidence). Large-scale gravity waves in the cloud layer exhibit both ascending and descending regions (see next section). The other combinations are weak and reflect mostly short-time fluctuations such as dissipating clouds. These other four octants are not negligible in horizontal coverage but do not contribute to the vertical transport of momentum, heat, and moisture, whereas the first four octants do (see the details in section 3). The octant analysis can be directly applied to the nonfiltered variables, but the classification becomes noisy because of a lot of small-scale turbulent fluctuations, especially in the wind speed components, as illustrated in appendix A. It is thus an essential part of the analysis to first filter out the incoherent part of the flow for accurate tracking of the coherent structures. This method enables clear and continuous classification of flow patterns across the interface between the boundary and cloud layers and does not depend on a threshold. The different perturbations also have a direct translation into the contribution to the overall vertical transport, the main role of dry and moist convection.

## 3. Results

### a. Coherent and incoherent decomposition

Figure 3 shows the vertical profiles of horizontally ($x$–$y$ plane) and temporally (30 min) averaged liquid water potential temperature $\overline{\langle\theta_l\rangle}$; total water mixing ratio $\overline{\langle q_{\rm tot}\rangle}$; normalized decaying passive scalar $\overline{\langle s_1\rangle}$ and normalized nondecaying passive scalar $\overline{\langle s_2\rangle}$; and coherent turbulent kinetic energy (TKE), sum of incoherent and SGS TKE, and total TKE (sum of coherent, incoherent, and SGS TKE). Here, angle brackets and overbars indicate horizontal and temporal averages, respectively. A well-mixed boundary layer of $\overline{\langle\theta_l\rangle}$ and $\overline{\langle q_{\rm tot}\rangle}$ extends up to $z = \sim$0.6 km, and a cloud layer appears from the top of the boundary layer up to $z = \sim$1.44 km (Figs. 3a,b) and is capped by the "trade inversion" layer, which extends up to $z = \sim$2 km. The vertical profiles of two passive scalars illustrate the decaying and nondecaying characteristics of the two scalars, respectively. The concentration $\overline{\langle s_1\rangle}$ abruptly decreases in the lower boundary layer (including the surface layer) and then decreases more slowly above, indicating intense turbulent mixing in the boundary layer and reduced turbulence in the cloud layer. In contrast to $\overline{\langle s_1\rangle}$, $\overline{\langle s_2\rangle}$ increases

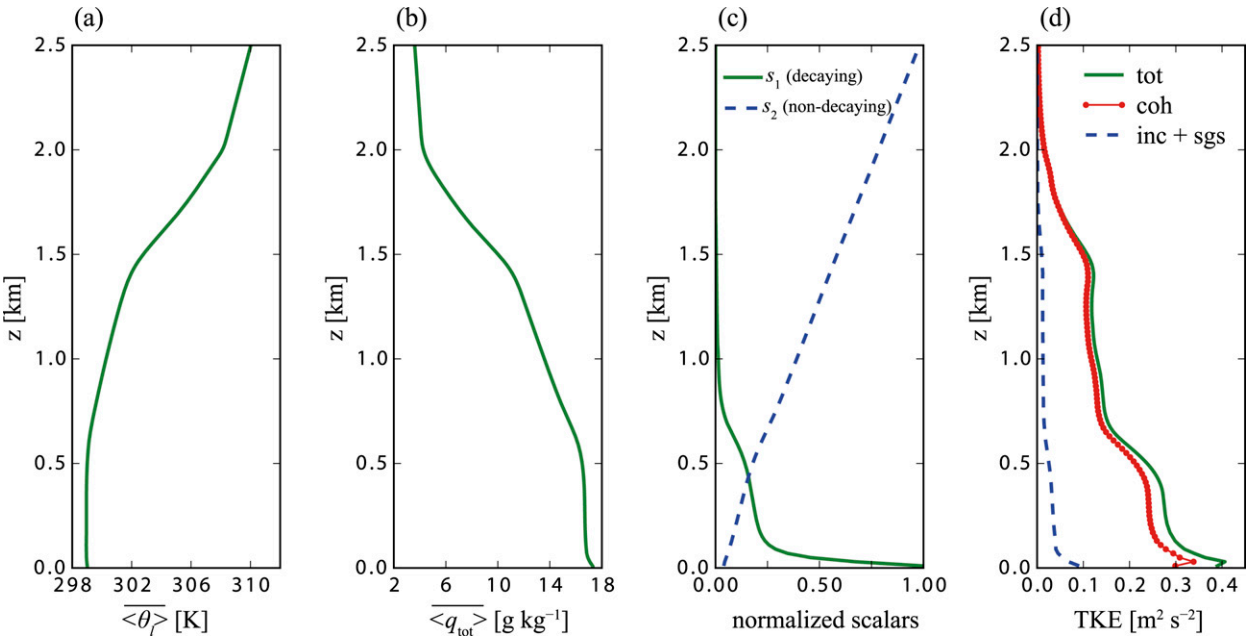


FIG. 3. Profiles of horizontally and temporally (30 min) averaged (a) liquid water potential temperature, (b) total water mixing ratio, (c) decaying and nondecaying passive scalars, and (d) coherent, sum of incoherent and subgrid-scale TKE, and total TKE.

monotonically with height and maintains the initial distribution as we intended with the short relaxation time scale. The coherent TKE (defined as half the sum of squared coherent velocity horizontal perturbations) retains most of the total TKE (76.7%–98.7%), while the sum of incoherent and SGS TKE is nonnegligible (more than ~10% of total TKE) in the lower boundary layer.

Figure 4 shows the horizontal cross section of total, coherent, and incoherent vertical velocity at $t = 21\,600$ s and $z = 350$, 850, and 1450 m. Contours of 0.01 g kg$^{-1}$ liquid water mixing ratio are added in Fig. 4 to show horizontal distribution of condensed water clouds. Strong updrafts and weak downdrafts appear in the middle of the boundary layer (Fig. 4a). The updrafts are arranged in near-parallel lines following mean horizontal wind direction (82.1° at $z = 350$ m). These types of aligned updrafts are known as streaks or ascending parts of convective rolls (LeMone 1973; Moeng and Sullivan 1994), and they appear as low-speed regions in the horizontal velocity components (not shown).

Cloudy updrafts, born from subcloud horizontal streaks, grow up into the cloud layer (Fig. 4d), and some of them reach the upper cloud layer (Fig. 4g). Circular convective updrafts in the lower cloud layer (at $z = 850$ m) spread over the subcloud convective rolls and carry most of the water that condenses above the condensation level (Fig. 4d). While the cloudy updrafts in the lower cloud layer still present a horizontally elongated structure, in the upper cloud layer (at $z = 1450$ m) the updrafts tend to exhibit a thermal-like structure and their spatial and temporal distribution tend to be more intermittent and more patchy (Fig. 4g).

Coherent vertical velocity fields (i.e., obtained with CVE filtering) are smoother than the original total fields. This smoothing, which corresponds to denoising, makes the octant classification efficient (see also appendix A). In contrast, the incoherent vertical velocity fields are mostly due to random perturbations, which are spatially decorrelated in the boundary layer (Fig. 4c), and limit the detection of coherent structures. In the cloud layer, most of the incoherent turbulence is present around cloudy regions since the air far away from clouds is nearly nonturbulent (Figs. 4f,i) and clouds are the main source of TKE.

As updrafts rise in the free-tropospheric stable stratification, they generate gravity waves. Vertical momentum transport by gravity waves is determined by their scales, and small-scale gravity waves do not transport momentum in the vertical direction (Kershaw 1995). As seen in Fig. 4, gravity waves are also decomposed into coherent and incoherent parts. The large-scale (transporting) gravity waves are classified as the coherent part while the small-scale (nontransporting) gravity waves are classified in the incoherent vertical velocity fields and are thus conveniently filtered out in the coherent part. In the cloud layer, large ascendance or subsidence regions can be observed, corresponding to those larger gravity waves (Fig. 4). On average, in the

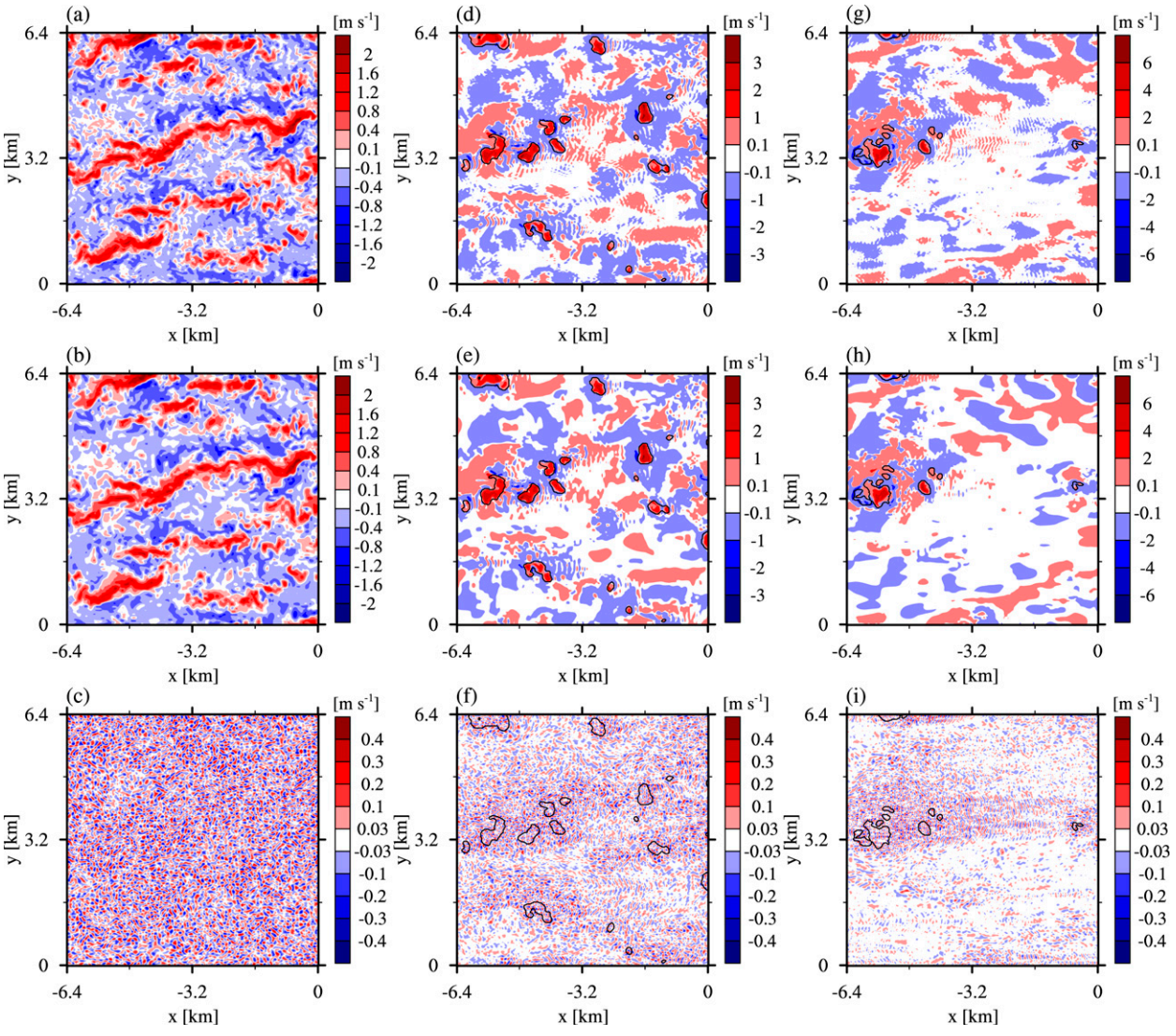


FIG. 4. Fields of (a) total, (b) coherent, and (c) incoherent vertical velocity at $t = 21\,600$ s and $z = 350$ m and the same fields at $z =$ (d)–(f) 850 and (g)–(i) 1450 m. The contours of 0.01 g kg$^{-1}$ liquid water mixing ratio are added in (d)–(i). The northwestern quarter of the horizontal domain is shown for clarity.

horizontal there is not much contribution to the momentum and temperature transport from the gravity wave, as is discussed below, as the ascending and descending motions nearly compensate each other.

Figure 5 shows the horizontal cross section of coherent liquid water potential temperature, coherent total water mixing ratio, and coherent decaying scalar at $t = 21\,600$ s and $z = 350$, 850, and 1450 m. The adiabatically conserved liquid water potential temperature also displays convective structures well. In the boundary layer, low and high $\theta_l^c$ correspond to updraft (indicated by red contours) and downdraft, respectively, each bringing cooler air from below and warmer air from the cloud layer (Fig. 5a). Cloudy updrafts are distinct at $z = 850$ and 1450 m (Figs. 5b,c) and exhibit strong negative anomalies of $\theta_l^c$.

The moisture field in the boundary layer shows the line-arranged updrafts with high humidity anomalies (Fig. 5d). Those high–mixing ratio streak regions in the boundary layer are generally connected to the cloudy updrafts at $z = 850$ m in the lower cloud layer (Fig. 6b). The cloudy updrafts are surrounded by high-$q_{\rm tot}^c$ regions, which decay slowly in time and increase the moisture in the environment as time goes on (Figs. 5e,f).

The distribution of coherent decaying scalar $s_1^c$ (Figs. 5g–i) is quite similar to that of total water mixing ratio (Figs. 5d–f), except that the fields of decaying scalar are less oversaturated and less diffused in the

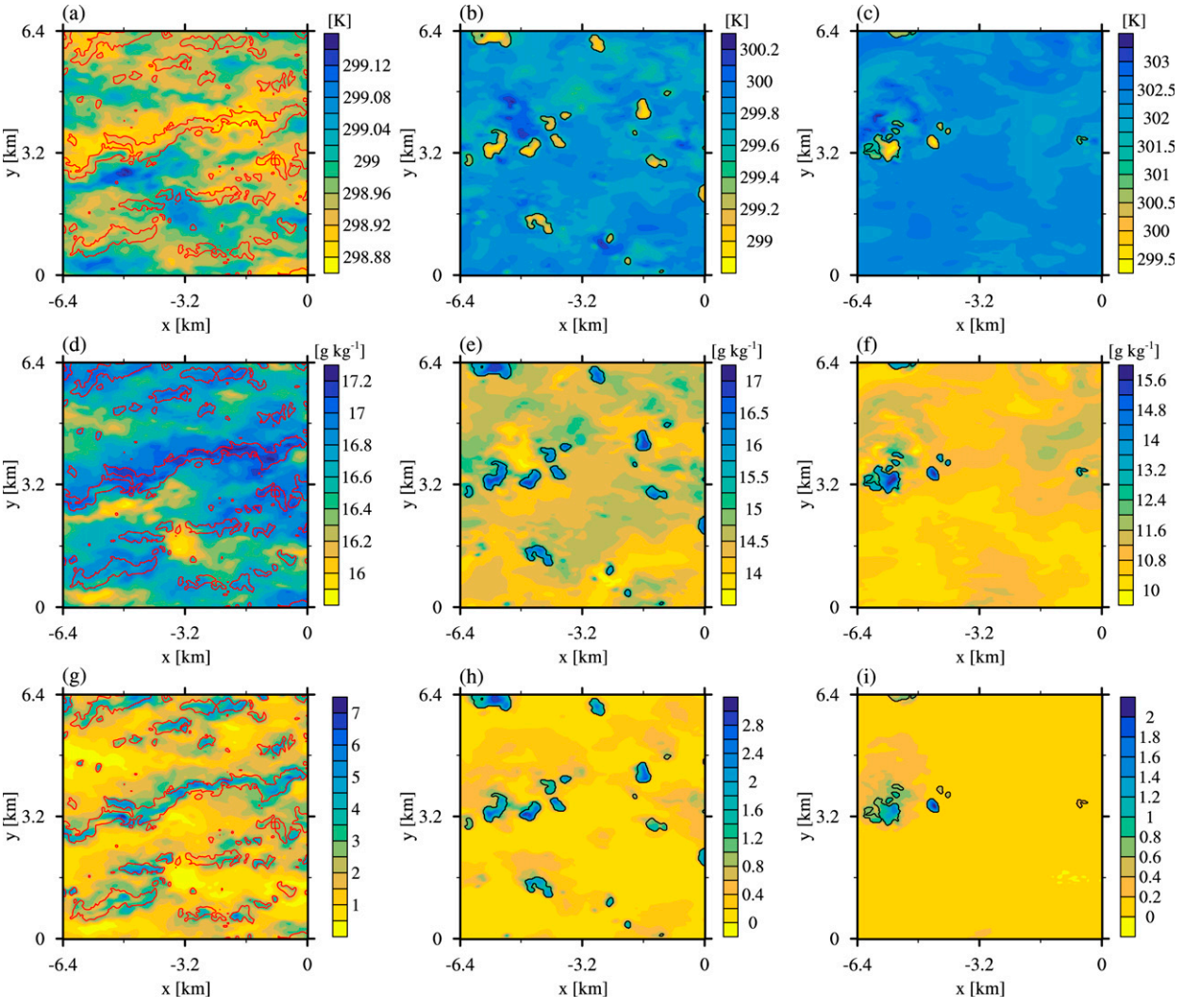


FIG. 5. Fields of coherent liquid water potential temperature at $t = 21\,600$ s and at $z =$ (a) 350, (b) 850, and (c) 1450 m. (d)–(f) Fields of coherent total water mixing ratio and (g)–(i) fields of the coherent decaying scalar. The black contours of 0.01 g kg$^{-1}$ liquid water mixing ratio and red contours of 0.4 m s$^{-1}$ vertical velocity are added. The northwestern quarter of the horizontal domain is shown for clarity.

environment, allowing better tracking of the updraft and subsiding shell structures. The scalar decay clearly delineates the convective updrafts from the environment (Couvreux et al. 2010; Rio et al. 2010). The other passive scalar $s_2^c$ shows a distribution opposite to that of $s_1^c$ (not shown).

Figure 6 shows a vertical cross section in the $x$–$z$ plane (at $y = 3337.5$ m) of the coherent vertical velocity, coherent total water mixing ratio, coherent decaying scalar $s_1^c$, and coherent nondecaying scalar $s_2^c$. Convective structures composed of updrafts and subsiding shells are seen in the field of vertical velocity (Fig. 6a). Two cloudy updrafts, centered at $x = -5.4$ and $x = -4.5$ km, develop upward into the inversion layer and several weaker updrafts, centered at $x = -3.7$, 0, and 0.6 km, appear in the cloud layer. Moisture and decaying scalar tend to concentrate in the boundary layer, streaklike, updrafts. A small fraction of those updrafts goes up into the cloud layer as thermal structures (Figs. 6b,c). The field of nondecaying scalar $s_2^c$ clearly illustrates the upward transport of scalar by updrafts, as a strong negative anomaly in the $s_2^c$ field (Fig. 6d). The initial profile of the nondecaying scalar is set to the corresponding height; thus, in the absence of lateral entrainment, the value of the nondecaying scalar directly reflects the initial position of the air. The entrainment into the clouds, across lateral boundaries, especially around the two strong updrafts, is nicely observable in Fig. 6d, as air from lower levels penetrates into the cloud layer but is diluted around the edges of the clouds (Heus et al. 2008).

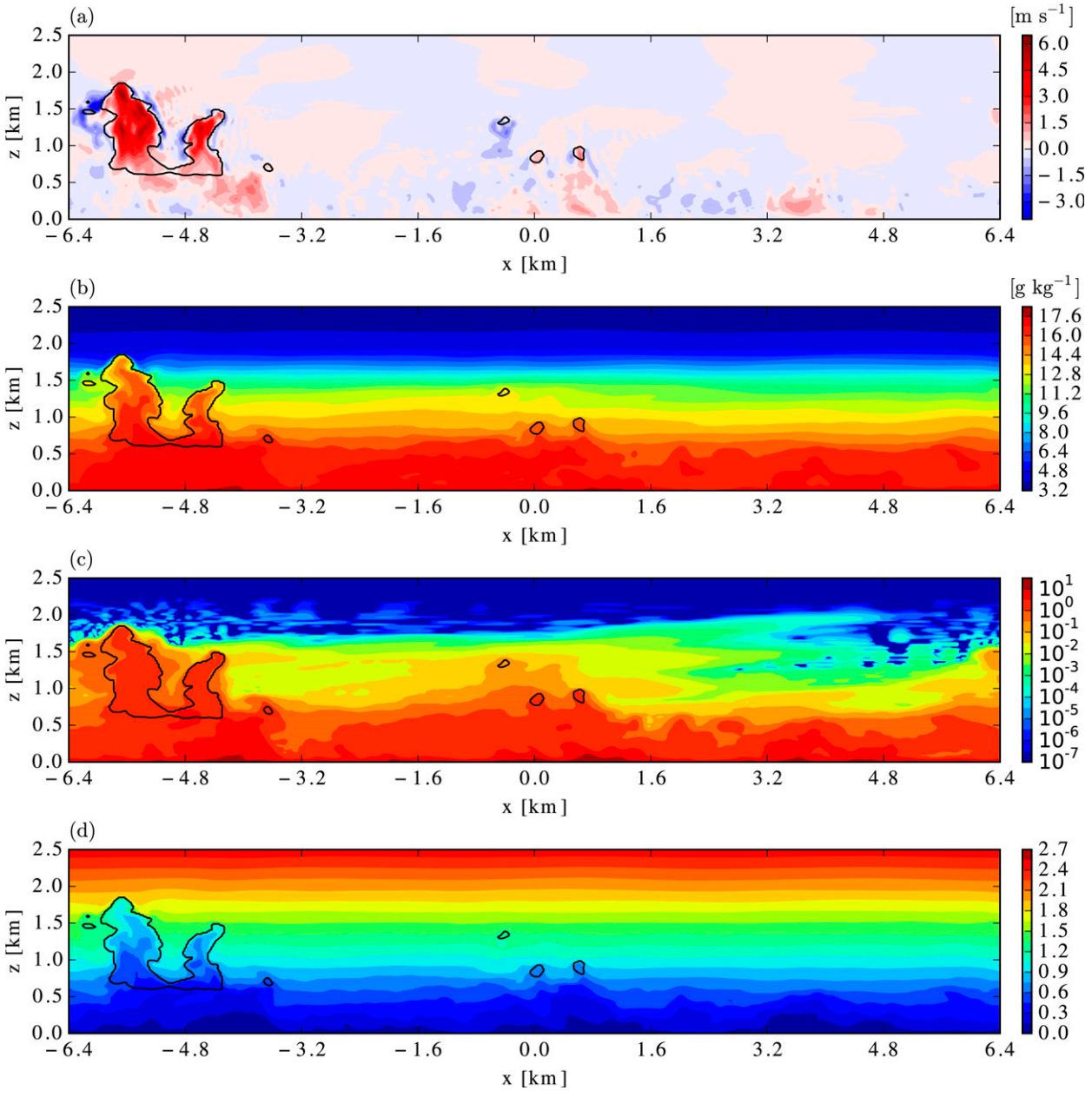


FIG. 6. Fields of (a) coherent vertical velocity, (b) coherent total water mixing ratio, (c) coherent decaying scalar, and (d) coherent nondecaying scalar in the $x$–$z$ plane at $y = 3337.5$ m. The contours of 0.01 g kg$^{-1}$ liquid water mixing ratio are added.

Figure 7 shows the one-dimensional $k_x$ spectra of vertical velocity and total water mixing ratio at $t = 21\,600$ s and $z = 350$, 850, and 1450 m. The $x$-directional spectra of total, coherent, and incoherent components of each variable are calculated at every $y$ position, and all calculated spectra are averaged in the $y$ direction. The spectra of the coherent parts cover most of the total spectral variance, especially at low wavenumber [i.e., at large scales ($\gtrsim$100 m)], while the spectra of the incoherent part retain most of total spectral variance at the small scales ($\lesssim$100 m). This behavior is observed in the boundary layer at $z = 350$ m (Figs. 7a,d), in the lower cloud layer at $z = 850$ m (Figs. 7b,e), and in the upper cloud layer at $z = 1450$ m. The spectra of liquid water potential temperature and the two passive scalars are similar to those of total water mixing ratio (not shown). This indicates that coherent (incoherent) parts are dominant at large (small) scales, but both are multiscale in nature as they spread over a wide range of wavenumbers. The coherent part contains most of the larger-scale

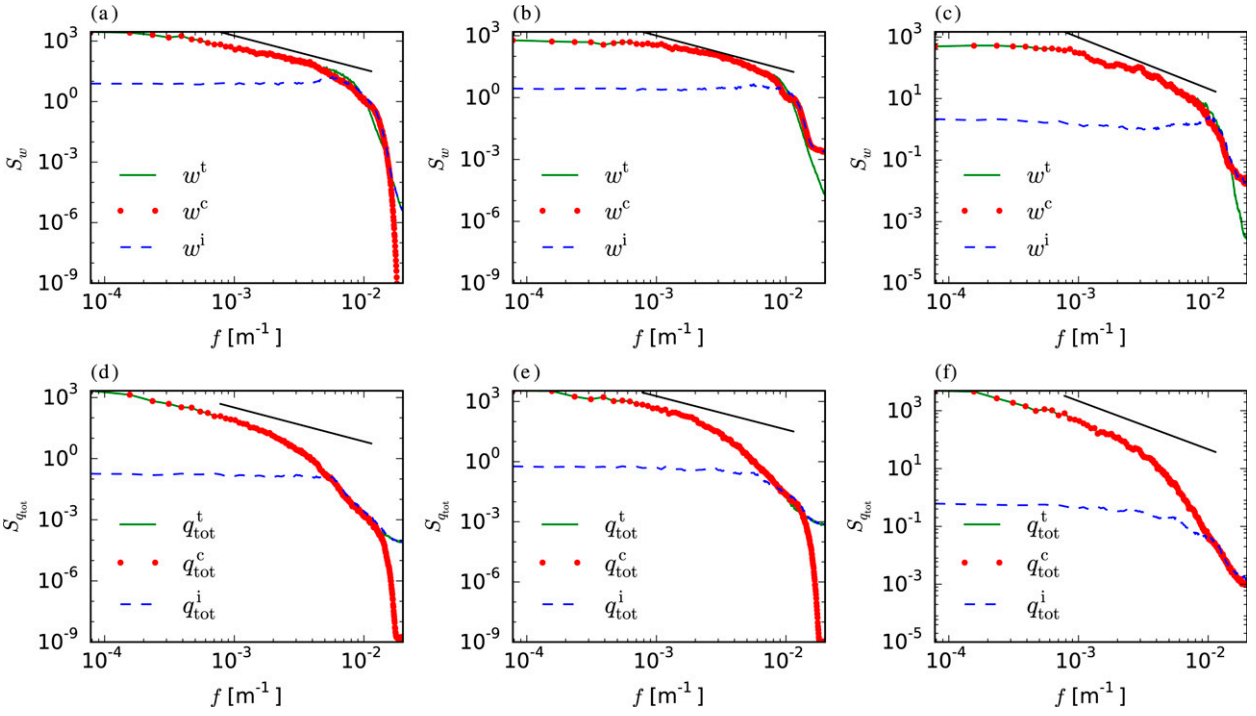


FIG. 7. Spectra of total, coherent, and incoherent vertical velocity at $z$ = (a) 350, (b) 850, and (c) 1450 m, and those of total water mixing ratio at $z$ = (d) 350, (e) 850, and (f) 1450 m. Black lines of −5/3 slope are added.

energy-containing and inertial-subrange eddies (Fig. 7), as has been found for homogeneous isotropic turbulence (Farge et al. 2001; Kadoch et al. 2011; Okamoto et al. 2011b). The incoherent part, on the other hand, exhibits a flat spectrum, characteristic of white noise, except close to the subgrid-scale filtering wavenumber, because of inherent spectral limitation wavelength cutoff due to the subgrid-scale length scale imposed by the Nyquist frequency. This flat spectrum of the incoherent part corresponds to energy equipartition between the different scales, and in physical space this indicates that the field is indeed uncorrelated. As small scales are mostly incoherent, the LES subgrid-scale model acts as a filter of the incoherent part of the flow. High-resolution turbulent models, such as direct numerical simulations, thus exhibit a large incoherent spectrum (Farge et al. 2001), and the coherent decomposition is essential as the LES resolution increases.

### b. *Coherent spatial structures*

An example of the octant analysis of the coherent part of the vertical velocity, decaying scalar, and non-decaying scalar at $t$ = 21 600 s and $z$ = 350, 850, and 1450 m is shown in Fig. 8. The second octant reflects the updraft, the third octant reflects the ascendance, the sixth octant reflects the downdraft/shell, and the seventh octant reflects the subsidence. The distribution of those four octants illustrates the boundary layer streaks composed of line-arranged updrafts, surrounded by downdrafts/subsiding shells. Between those structures, subsidence dominates (McNaughton and Brunet 2002), and this alternating pattern of updraft versus subsidence reflects the typical ejection–sweep mechanism observed in the surface layer (Katul et al. 1997; Lin 1999; McNaughton and Brunet 2002; Kim and Park 2003; Watanabe 2004; Foster et al. 2006; Katul et al. 2006; Guingo and Minier 2008; Zeri and de Abreu Sá 2011). We note that the downdrafts/subsiding shells around the streaks cannot be due to buoyancy sorting, which is typically used as the explanation of the subsiding shells for updrafts (Heus and Jonker 2008; Abma et al. 2013), as there is no phase change in the boundary layer. Instead, the buoyancy of the downdrafts/subsiding shells is very similar to that of the updrafts (Fig. 13) and the downdrafts/subsiding shells in the boundary layer are mostly the returning part of a vortex-like structure (similar to Hill's vortex). We note that the updraft–subsidence organization in the boundary layer reflects the perspective of Bjerkness (1938) of shallow convection with narrow updrafts surrounded by widespread slow subsidence between them.

Above the boundary layer, we observe more-circular, thermal-like, updrafts surrounded by downdrafts/subsiding shells, as previously noticed in isolated clouds

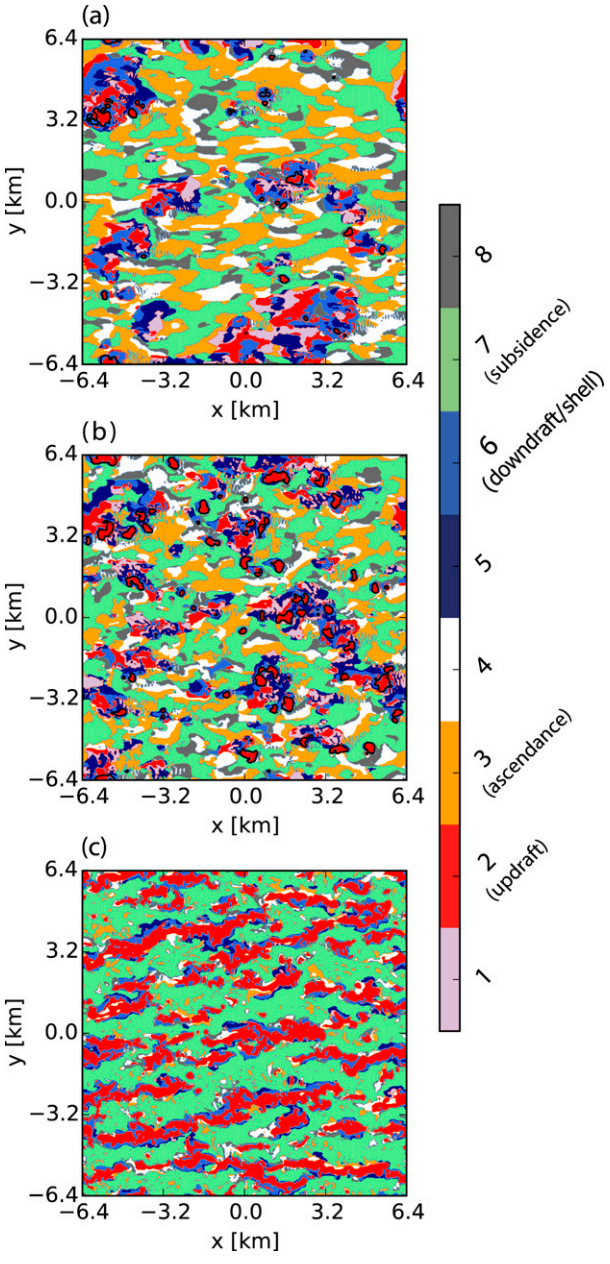


FIG. 8. Fields of octants at $t = 21\,600$ s and at $z =$ (a) 1450, (b) 850, and (c) 350 m. The contours of 0.01 g kg$^{-1}$ liquid water mixing ratio are added in (a) and (b).

(Heus and Jonker 2008; Abma et al. 2013). Most of the strong updrafts have condensed water, and the downdrafts/subsiding shells are mostly cloud-free (outside of black contour lines), as earlier realized with a linear theoretical analysis by Bretherton (1987) and further confirmed by high-resolution turbulent simulations looking at individual clouds (Heus and Jonker 2008; Abma et al. 2013). Downdrafts/subsiding shells in the boundary and cloud layers can be quite extensive spatially, especially in regions with multiple updrafts (see below). The downdrafts/subsiding shells are much denser than the updrafts (Fig. 13), and the buoyancy anomaly increases as the updrafts rise into the cloud layer and the anomaly peaks at the bottom of the inversion layer. This means, as previously noted (Heus and Jonker 2008; Abma et al. 2013), that decreased buoyancy in subsiding shells induced by evaporative cooling is substantial and accelerates the subsiding shells downward.

In the cloud and inversion layers, the ascendance octant becomes more prevalent than in the boundary layer yet does not contribute much to the total transport (see section 3c). This ascendance is induced by gravity waves, and the overall coverage of the ascendance is equivalent to the subsidence region (see section 3c). In the upper cloud layer ($z = 1450$ m), strong updrafts with condensed water rise from below and are surrounded by downdrafts or subsiding shells (Fig. 8a). The updrafts and downdrafts are connected as large structure (several-kilometer scale). The structures are composed of active updrafts and dissipating flow structures. Gravity waves (as detected by the ascendance and subsidence octants), which are transporting momentum, are detected around the large convective structures. The environmental ascendance and environmental subsidence are frequent outside the connected convective structures at $z = 850$ and 1450 m. The connected updraft structures are larger higher in the inversion layer (e.g., at $z = 1450$ m compared to $z = 850$ m), because of the entrainment or aggregation of smaller structures. It is also notable that several downdrafts appear quite separated from convective structures at $z = 1450$ m. This can be attributed to the dissipating updrafts and top-down (penetrative) downdrafts, which are longer lived than the active updrafts.

Figure 9 shows a vertical cross section in the $x$–$z$ plane (at $y = 4412.5$ m) of the octants (Fig. 9a), coherent vertical velocity (Fig. 9b), perturbation of coherent liquid water potential temperature (Fig. 9c), and perturbation of coherent total water mixing ratio (Fig. 9d). The strength of the eight flow patterns and their roles can be illustrated by comparing the fields of octants and the magnitudes of vertical velocity, temperature perturbation, and moisture perturbation in Figs. 9b–d. Updrafts and downdrafts/shells are distinct, and environmental subsidence is weak but frequent. Updrafts and subsidence in the boundary layer are associated with larger-scale upward and downward convective structures, comprising convective rolls tilted in the mean-wind direction (Fig. 4). The boundary layer updrafts/streaks are directly connected to cloudy updrafts, transporting moisture from the boundary layer to the cloud layer

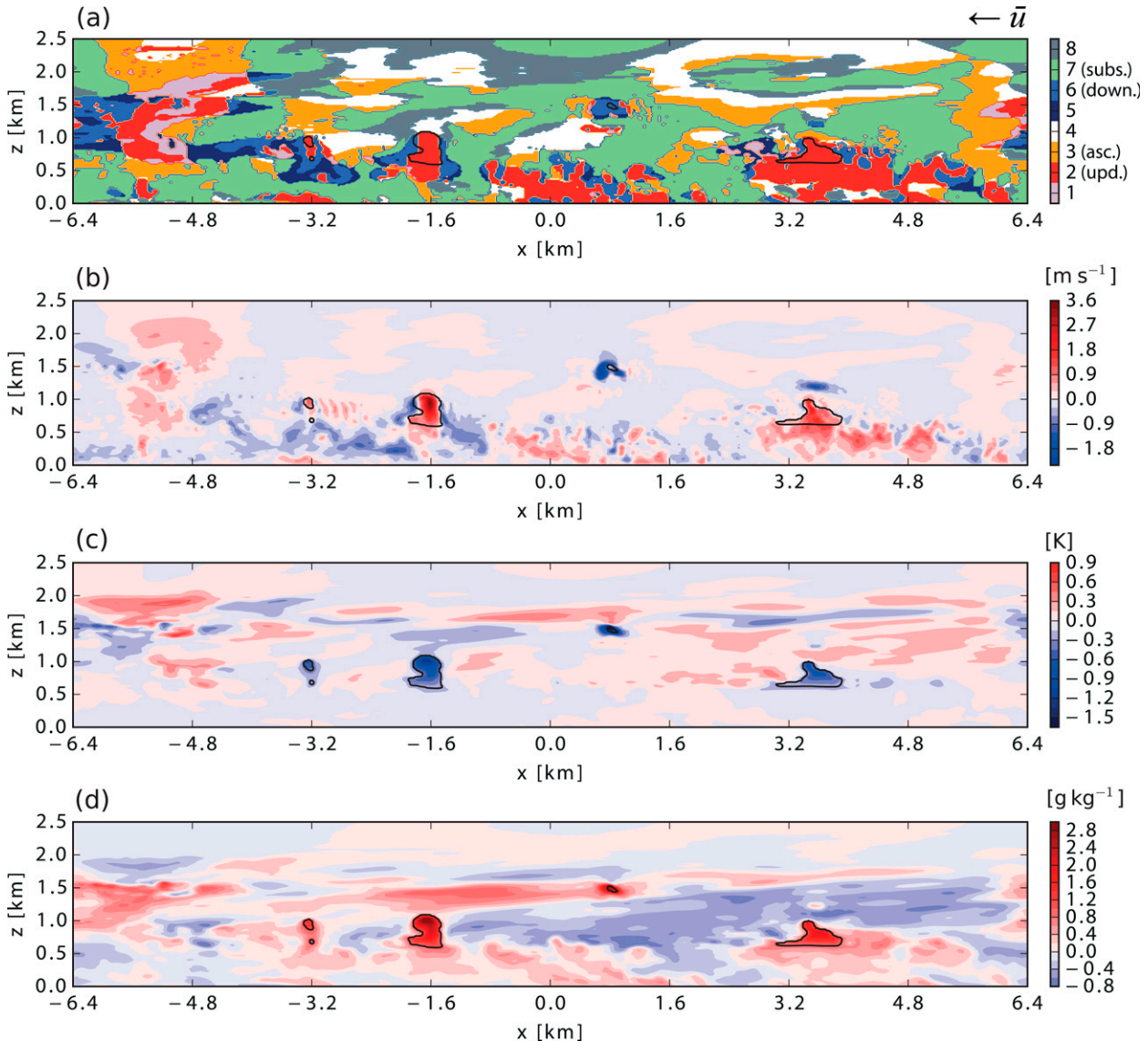


FIG. 9. Fields of (a) octants, (b) coherent vertical velocity, (c) perturbation of coherent liquid water potential temperature, and (d) perturbation of coherent total water mixing ratio in the $x$–$z$ plane at $y = 4412.5$ m. The contours of 0.01 g kg$^{-1}$ liquid water mixing ratio are added.

(Fig. 9d). The connection between the updrafts in the boundary layer and those in the cloud layer is, however, sporadic, and the entire streak does not become a cloudy updraft; only a smaller subregion with the highest water content, and therefore lower level of free convection, is extracted from the streaks and becomes a cloudy updraft. Strong updrafts in the cloud layer are typically associated with downdrafts/subsiding shells (Fig. 9a), and the downdrafts/subsiding shells can be sometimes cloudy, as seen for instance at $x = -1.6$ km and $z = 1.2$ km, confirming the vortex ring structure of cloudy updrafts (Sherwood et al. 2013).

The cloudy updrafts carry most of the moisture, and moisture inside the cloudy updrafts concentrates in the center of the updrafts (Fig. 9d), indicating again internal circulation similar to Hill's vortex (Bretherton 1987; Sherwood et al. 2013). It is also notable that cloudy updrafts and downdrafts, such as the ones appearing at $x = \sim 0.8$ km and $z = \sim 1.5$ km can be part of a dissipating flow structure similar to "passive clouds" (Stull 1988). The weak updraft in the inversion layer at $x = \sim -5$ km and $z = 2$ km is another example of the dissipating flow structures in the inversion layer. This passive flow structure can be clearly seen in the field of moisture

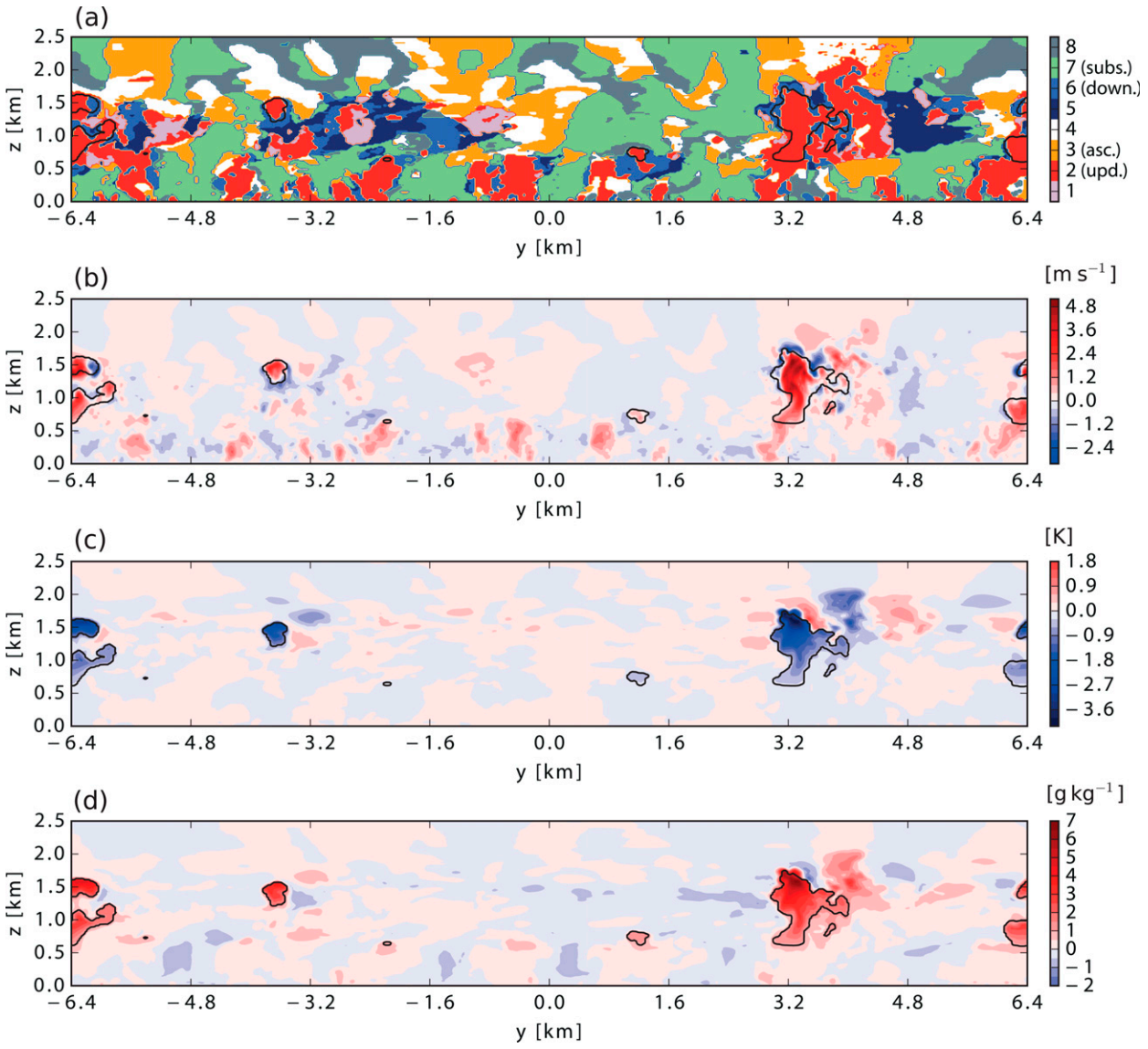


FIG. 10. Fields of (a) octants, (b) coherent vertical velocity, (c) perturbation of coherent liquid water potential temperature, and (d) perturbation of coherent total water mixing ratio in the $y$–$z$ plane at $x = -5512.5$ m. The contours of 0.01 g kg$^{-1}$ liquid water mixing ratio are added.

(Fig. 9d), as it has a strong positive moisture anomaly yet a very weak velocity. Those passive clouds would typically not be detected by other methodologies yet would have an impact on the radiation field if they were to be interactive. The moisture field shows weak but streamwise-elongated structures in the cloud and inversion layer. This is related to turbulent mixing around the strong cloudy updrafts and advection of slowly dissipating convective structures, as described in appendix C. Nonetheless, updrafts are more clearly associated with localized perturbations in liquid potential temperature and moisture, contrary to virtual potential temperature, which is smoothed out by gravity waves transporting buoyancy but not moisture.

A vertical cross section in the $y$–$z$ plane (at $x = -5512.5$ m) of the octants, coherent vertical velocity, perturbation of coherent liquid water potential temperature, and perturbation of coherent total water mixing ratio is plotted in Fig. 10. The updrafts, comprising the horizontal streaks and convective rolls in the boundary layer (Fig. 4), appear side by side, and some of them extend through the cloud layer, while others are suppressed by environmental subsidence in the surface layer or by stability in the cloud layer. The spanwise

spacing between the convective structures depends on the vertical size of corresponding convective structures. For instance, the spacing is about several hundreds of meters between horizontal streaks, and the distance between the ascending branches of convective rolls is more than twice the boundary layer height. The vertical transport of heat and moisture by cloudy updrafts is illustrated in Figs. 10c and 10d. One interesting point is that the strongest updraft at $y = 3.2$ km and $z = 1.5$ km is located beside the northern (right-hand side of the figure) dissipating flow structure, which corresponds to the dissipating flow structure shown in Fig. 9. Convective structures develop vertically, and several of them dissipate together, inducing a subtle mixture of updrafts and downdrafts. This kind of development–dissipation process is suspected to be the essential mechanism of entrainment and detrainment of plumes and will be investigated by tracking individual convective structures in future studies.

### c. *Contribution of coherent structures to transport*

The scatterplots of the eight octants in the $w^c$–$\theta_l^c$ plane and $w^c$–$q_{\text{tot}}^c$ plane at $z = 350$, 850, and 1450 m in Fig. 11 illustrate the frequency and magnitude of the octants. The updrafts are the strongest octant in terms of vertical velocity and scalar anomalies, contributing the most to vertical transport of heat and moisture in the cloud layer (Figs. 11a–d). The next strongest octant is the downdraft/shell that acts in the opposite vertical direction to the updrafts. The other octants are not clearly distinct in magnitude in the cloud layer. In the boundary layer, the magnitudes of perturbations are much smaller than those in the cloud layer as could be expected in a neutral stratification compared to a conditionally unstable stratification, where cloudy updrafts can substantially deviate from the environmental values because of latent heating. Updrafts and environmental subsidence are frequent, and they are comparable in terms of flux contribution (Figs. 11e,f) in the boundary layer. Downdrafts/subsiding shells and ascendance are also relatively frequent in the boundary layer but do not transport much. In the boundary layer (e.g., $z = 350$ m), the main contribution of the updrafts to the transport is due to the anomalies of vertical velocity but not to the scalar anomalies, which are fairly close to the environmental values. This reflects the acceleration and entrainment of the updrafts as they rise from the surface into the boundary layer. The updrafts accelerate but tend to reduce their scalar anomalies with the environment through entrainment as they rise. Subsidence conversely is typically slow but exhibits relatively higher scalar anomalies.

Using CVE together with the octant analysis method, we can, for the first time, evaluate the (horizontally and temporally averaged) profiles of frequency (horizontal coverage), vertical velocity (mass flux divided by density), and contribution of the different structures to the vertical fluxes of heat and moisture (Fig. 12). The same profiles conditionally sampled on ''cloud core,'' defined as the positive buoyant region where liquid water mixing ratio is higher than $0.01\,\text{g}\,\text{kg}^{-1}$ (Siebesma and Cuijpers 1995), are added in Fig. 12 for comparison. The updraft, downdraft/shell, and environmental subsidence are frequent in the boundary layer while ascendance induced by gravity waves is also frequent in the cloud layer (Fig. 12a). The updrafts and environmental subsidence are the dominant contributors to the mass flux and transport in the boundary layer. In the cloud and inversion layers, downdraft/shell and ascendance are also comparable in magnitude to the updrafts and subsidence. In the upper inversion layer and above it, the updrafts and downdrafts/subsiding shells are nearly absent, but ascendance and discordance generated by gravity waves are the most frequent structures.

The contribution of each structure to the vertical turbulent fluxes of heat and moisture is shown in Figs. 12c and 12d. The updrafts are the most dominant contributor to the transport of heat above the surface layer. Even if they are infrequent in the upper inversion layer, their contribution to the transport is large because they carry large scalar anomalies (Figs. 5, 11). The second most important contributor in the cloud layer is the downdraft/shell octant, which transports heat and moisture in the opposite direction to the updrafts. There is a clear difference between the cloud layer and the boundary layer, as in the latter subsidence covers a large fraction of the domain (as previously thought for moist convection) and strongly contributes to the transport. In the cloud and inversion layers, the subsidence and ascendance contribution to the transport nearly cancel each other, and most of the downward motion contribution is due to the subsiding shell, not to the environmental subsidence. The weak role of environmental subsidence in the cloud layer of trade wind shallow convection had been reported earlier (Heus and Jonker 2008; Jonker et al. 2008) but is here refined by systematically investigating its transport contribution. In fact, the subsidence transport is not negligible in the cloud and inversion layer, but the transport and mass flux is almost entirely compensated by the environmental ascendance, which is of the same amplitude, as both are induced by the same gravity waves. A clear differentiation between penetrative/overturning downdrafts and shells depends on height, but a clear separation is difficult because of three-dimensional complex flow

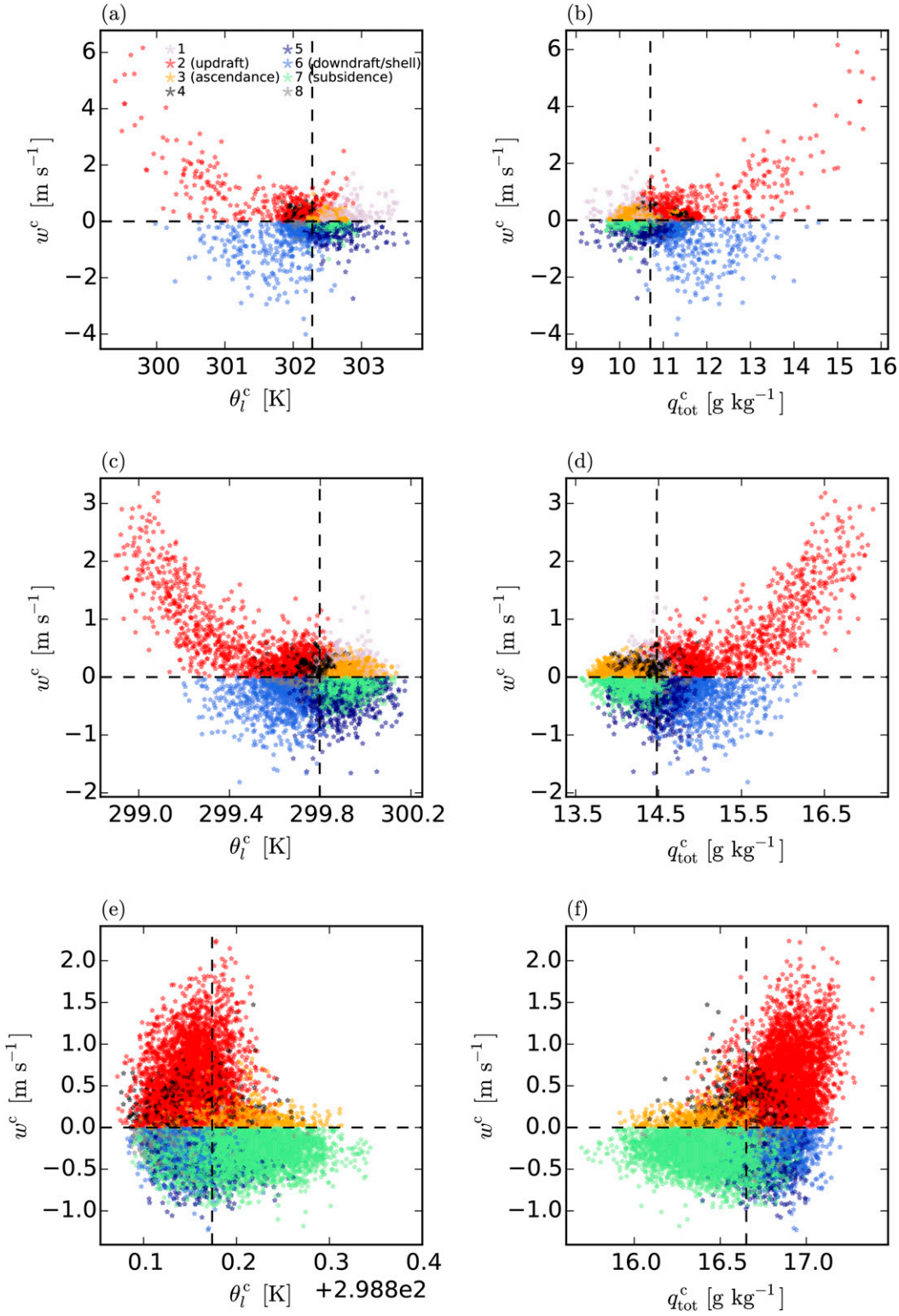


FIG. 11. Scatterplots of octants in the (a) $w^c$–$\theta_l^c$ plane and (b) $w^c$–$q_{tot}^c$ plane at $t = 21\,600$ s and at $z = 1450$ m and the same plots at $z =$ (c),(d) 850 and (e),(f) 350 m.

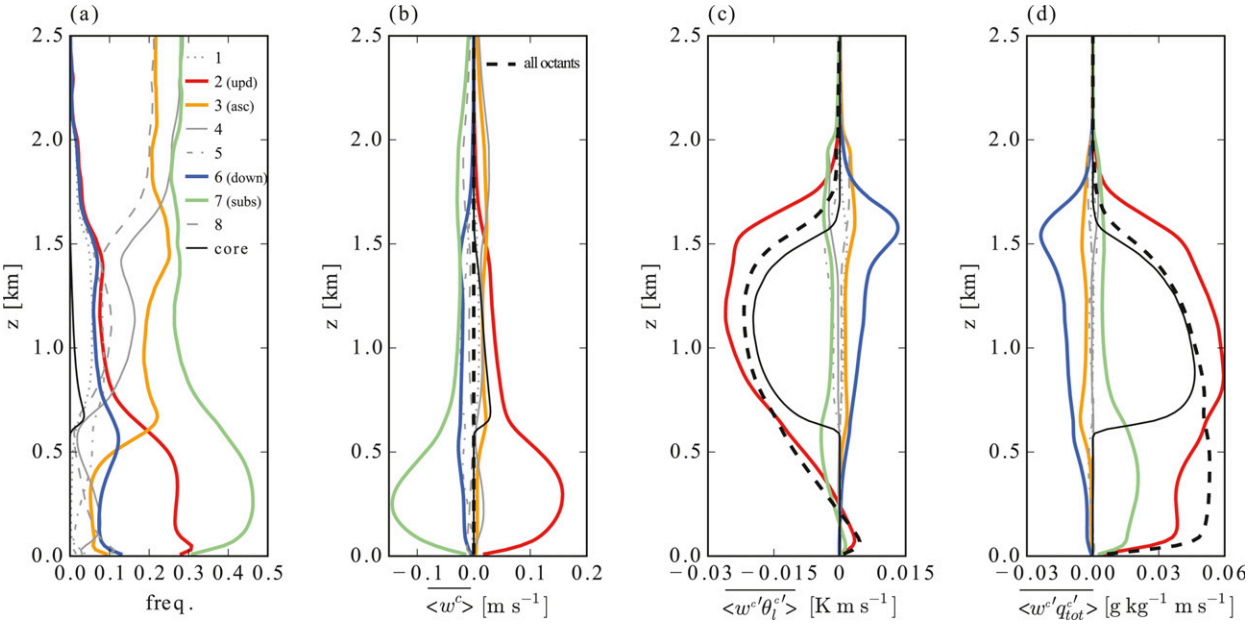


FIG. 12. Vertical profiles of horizontally and temporally (30 min) averaged (a) frequency, (b) vertical velocity, (c) vertical turbulent flux of liquid water potential temperature, and (d) vertical turbulent flux of total water mixing ratio of octants.

around updrafts. However, the buoyancy anomaly of the downdrafts is similar to that of the updrafts at the top of the inversion layer, suggesting that penetrative/overturning downdrafts are prevalent at the top of the inversion layer, whereas subsiding shells with evaporatively cooled buoyancy anomalies dominate in the lower inversion layer and the cloud layer (Fig. 13). This will be investigated further in a future study to understand the interaction between downdrafts and shells.

The role of the downdraft/shell is again illustrated in the profiles of $w^c$-weighted virtual potential temperature sampled in the updraft and the downdraft/shell, respectively (Fig. 13). To minimize the impact of dissipating weak updrafts, the sampled virtual potential temperature is weighted by coherent vertical velocity. The virtual potential temperature difference between the downdrafts/subsiding shells and the updrafts is small and of the same order in the boundary layer, this seems more plausible that the downdrafts/subsiding shells can be induced by the vortex-like circulation, a la Hill's vortex (Sherwood et al. 2013) at least in the boundary layer. It is also notable that the virtual potential temperature anomaly of downdrafts/subsiding shells is positive in the boundary layer (Fig. 13c). In the cloud layer, the virtual potential temperature anomaly of the updrafts (downdrafts) is positive (negative) compared to the environment. Downdrafts/subsiding shells exhibit strong negative buoyancy anomalies in the cloud layer, which illustrates the importance of evaporative cooling in the subsiding shells, as shown in the study of shallow convection (Heus and Jonker 2008; Jonker et al. 2008) and also deep convection (Glenn and Krueger 2014). We speculate that subsiding shells are generated by overturning circulations and that they are strengthened by evaporative cooling in the cloud layer.

Those results have important implications for the parameterization of dry and moist convection. In the boundary layer, updrafts and subsidence are the dominant contributors. Subsidence is an important transporter of moisture anomalies in the boundary layer, as it brings dry air from the cloud layer into the boundary layer. Thus, the concept of descending dry air through a wide environment (Bjerkness 1938) is more valid in the boundary layer than in the cloud layer. In the cloud layer, subsidence is not uniform around updrafts, does not transport much, and the transport is compensated by ascendance induced by the same gravity waves. Instead, downdrafts/subsiding shells are important contributors to the downward transport of scalars, especially in the inversion layer, where their transport contribution is comparable in magnitude to that of the updrafts. This means that downdrafts/subsiding shells have to be modeled in convective schemes and that the top-hat assumption is incorrect, because subsidence is not uniform and because subsiding shells are present around updrafts, altering the entrainment into updrafts (Heus and Jonker 2008; Jonker et al. 2008). In the boundary

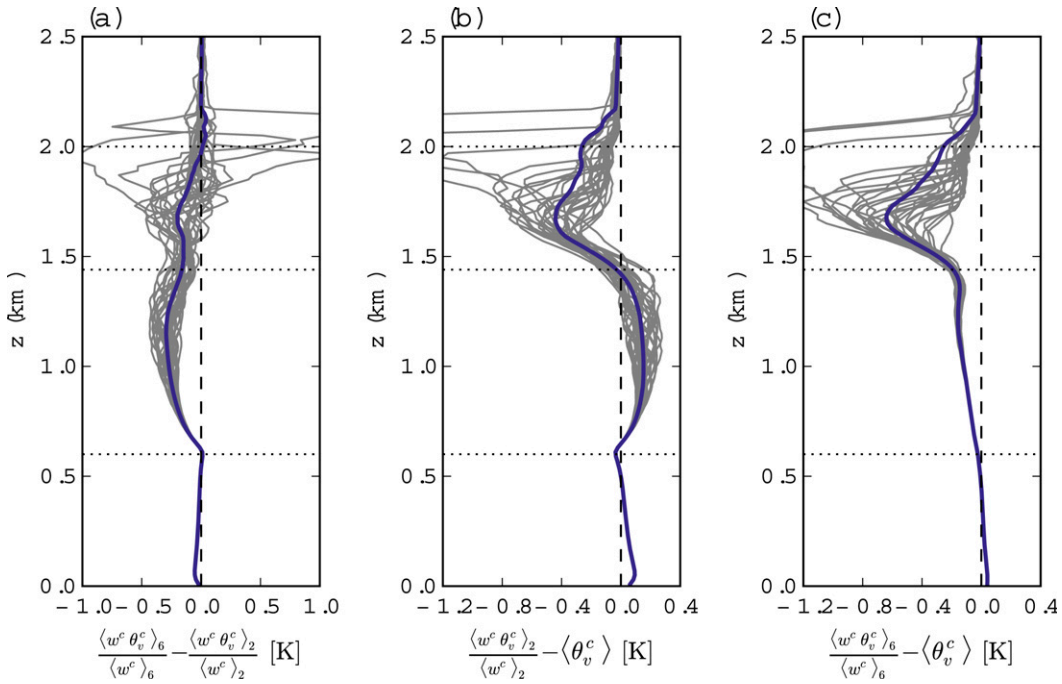


FIG. 13. Temporally (30 min) averaged profiles of (a) $w^c$-weighted $\theta_v^c$ of the downdraft/shell minus $w^c$-weighted $\theta_v^c$ of the updraft, (b) $w^c$-weighted $\theta_v^c$ of the updraft minus slab-averaged $\theta_v^c$, and (c) $w^c$-weighted $\theta_v^c$ of the downdraft/shell minus slab-averaged $\theta_v^c$. Profiles at each time instant are represented by gray lines. The three dotted horizontal lines indicate the tops of the boundary layer, the cloud layer, and the (trade) inversion layer, respectively.

layer, subsidence is an important contributor to the overall transport of heat and moisture but is not proportional to the updraft mass flux. This means that typical mass flux approaches should fail in the boundary layer and that subsidence [usually related to the entrainment process at the top of the boundary layer (Sullivan et al. 1998; McNaughton and Brunet 2002)] should be included in the parameterization of boundary layer transport (Gentine et al. 2013a,b).

### d. Coherent convective structures over land

Cumuli over the ARM SGP site are simulated for 9.5 h using the initial sounding, surface fluxes, and external forcing described in Brown et al. (2002). Octant fields at one $x$–$z$ plane ($y$ = 12.5 m) and three instants (3, 6, and 9 h) are presented in Fig. 14. Without spinup time, the octant fields can be calculated below the highest level reached by $s_1$ following updrafts. Thus, the vertical range of octants increases with time (e.g., from ~1.4 km at $t$ = 3 h to ~2.3 km at $t$ = 6 h). The octant fields show a complex and time-varying distribution of coherent structures from the boundary layer to the cloud layer. Boundary layer convective rolls appear at 3 h (0830 LT), shallow cumuli are seen at 6 h (1130 LT), and deeper cumuli develop far above the boundary layer at 9 h (1430 LT). The aggregated convective structures, mainly composed of updrafts and shells, appear again at 9 h, as seen in Fig. 10. The contribution of the octants to the vertical turbulent flux of moisture is also investigated (not shown). For example, updrafts, downdrafts/shells, and subsidence contribute 71%, −6.4%, and 37% of the vertical turbulent flux, respectively, at $z$ = 250 m and $t$ = 3 h. In the boundary layer this relative contribution is similar later in the simulation (6 and 9 h). In the cloud layer, updrafts, downdrafts/shells, and subsidence contribute 113%, −19%, and 15% of the vertical turbulent flux, respectively, at $z$ = 1550 m and $t$ = 9 h. Downdrafts/shells contribute more to the total flux in the cloud layer than in the boundary layer, and its contribution becomes larger in the inversion layer, similar to the BOMEX case (Fig. 12d). The contribution of the octants to the vertical turbulent flux of heat shows similar vertical distribution as in the BOMEX case (Fig. 12c). Overall, the results over this continental case are very similar to the BOMEX trade wind case, and the coherent structure extraction also performs very well in this case. Further study, focusing on continuous tracking of individual coherent structures, will help us understand the role of individual coherent structures in convection deepening and entrainment.

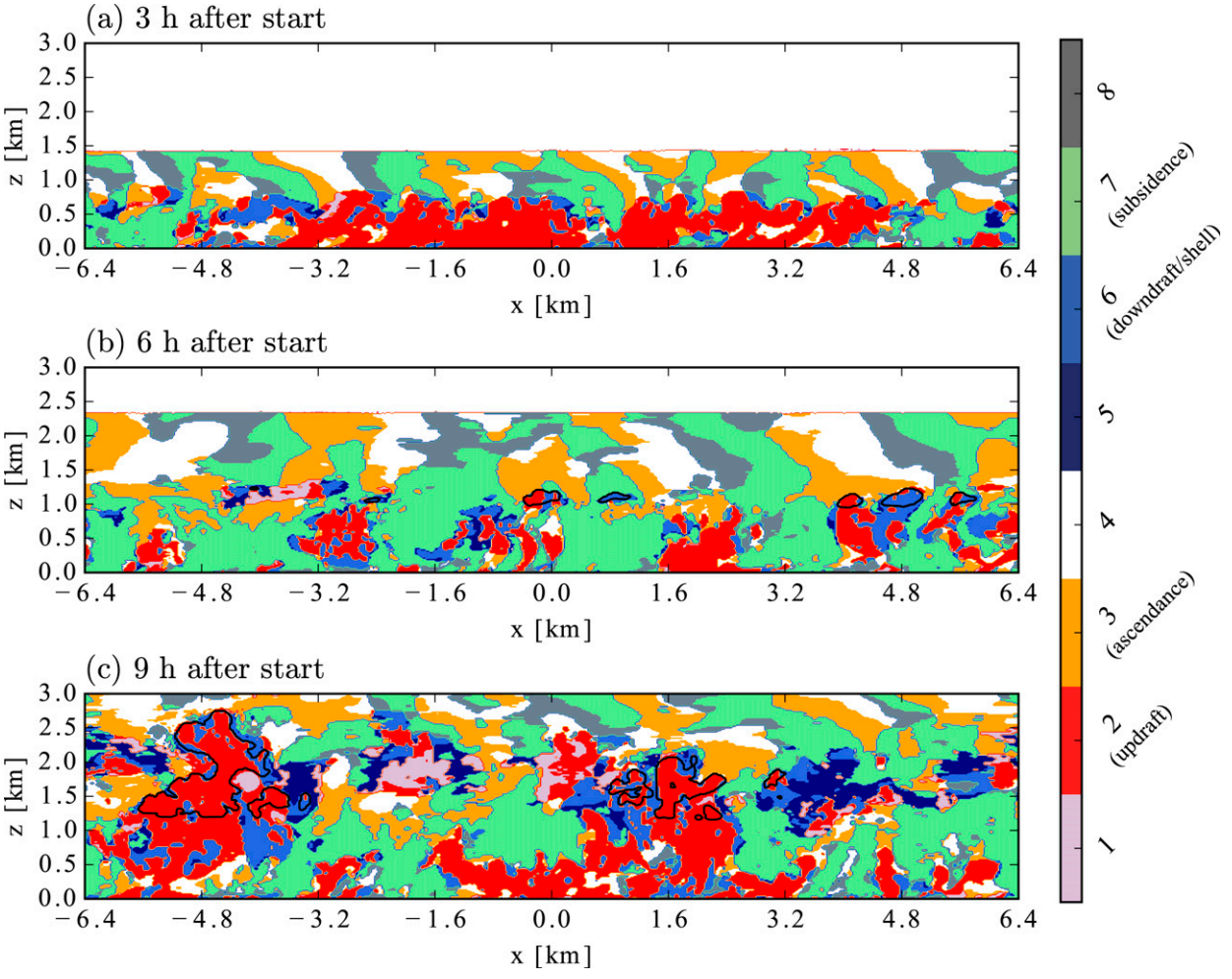


FIG. 14. Octant fields of $(w^c, s_1^c, s_2^c)$ at $y = 12.5$ m and $t =$ (a) 3, (b) 6, and (c) 9 h in the simulation of the ARM case. The contours of 0.01 g kg$^{-1}$ liquid water mixing ratio are added.

*e. A note on compression rate*

The efficiency of CVE filtering at $t = 21\,600$ s is illustrated in Fig. 2. Iteration number decreases from 7 near the surface to 3 above the surface layer. This indicates that the noise level also decreases with height in the lower boundary layer (and thus the turbulence level). The iteration number decreases again across the cloud layer and trade inversion, but the flow is weak, especially outside the narrow convective structures. The denoised coherent flow conserves most of the original vertical turbulent momentum flux (Fig. 2b) in all layers. However, it should be noted that the magnitude of the momentum flux above the cloud layer is much weaker than below. The denoised coherent flow and coherent total water mixing ratio also conserve most of the original vertical turbulent moisture flux (Fig. 2c). The ratio of coherent to total (resolved) vertical turbulent fluxes of other variables are checked, and the ratios of the energy contained are always above 95% (not shown). CVE and wavelet decomposition has the advantage that it can explain coherent flow and the total transport using only a very small number of wavelet coefficients, as Yano et al. (2004) reproduced more than 90% of variance in deep convection by retaining only the top 10% of the wavelet coefficients. The compression rate of the velocity components, defined as the ratio of the number of coherent wavelet coefficients to that of total wavelet coefficients, is shown in Fig. 2d. Above the surface layer, less than 10% (typically 5%–7%) of the wavelet coefficients represent the coherent flow and retain most of the flow structure and most of the transport. The four scalars $\theta_l^c$, $q_{\rm tot}^c$, $s_1^c$, and $s_2^c$ have likewise good compression rates, less than 10% (typically 5%–7%) in the wavelet domain above the surface layer (where the subgrid-scale LES contribution to the total flux is large) (Fig. 2d).

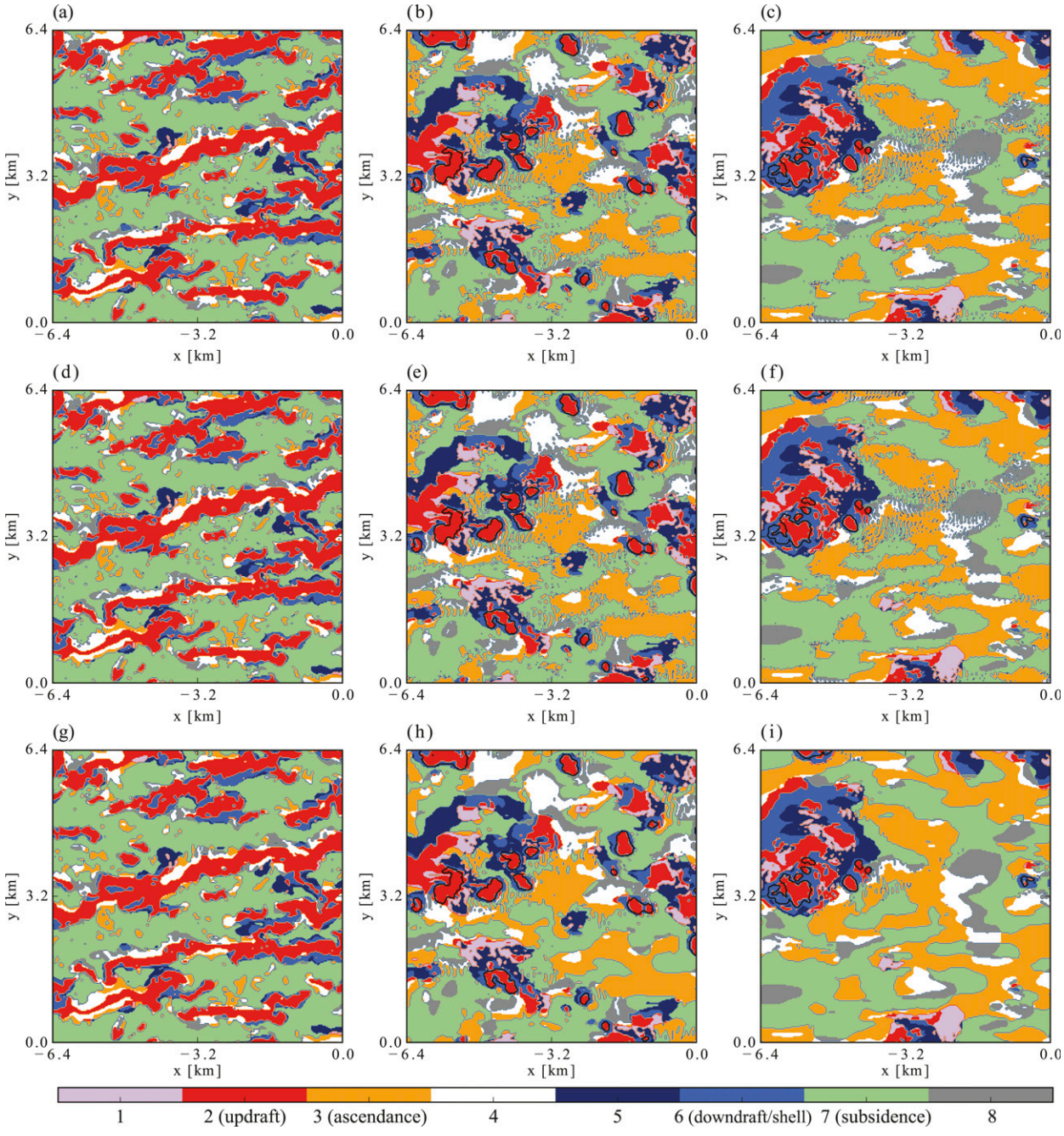


FIG. A1. Octant fields of $(w, s_1, s_2)$ at $t = 21\,600$ s and at $z =$ (a) 350, (b) 850, and (c) 1450 m; (d)–(f) octant fields of $(w, s_1^c, s_2^c)$; and (g)–(i) octant fields of $(w^c, s_1, s_2)$. The contours of 0.01 g kg$^{-1}$ liquid water mixing ratio are added at $z = 850$ and 1450 m.

Thus, the CVE filtering method based on the ratio of momentum flux is well adapted and efficient to describe shallow convection transport.

In cumulus parameterization a form of compression to represent convective transport is the so-called superparameterization method. Superparameterization is a method that explicitly resolves moist convections in a small sample of the GCM grid using an embedded cloud-resolving model (Khairoutdinov and Randall 2001; Khairoutdinov et al. 2005; Arakawa et al. 2011). Although its explicit calculation demands much more computing resources than the standard convective parameterization, such as the bulk mass flux approach, it has shown great potential because of its improved predictability of local and global climate that are closely related to convection-scale phenomena (Li et al. 2012).

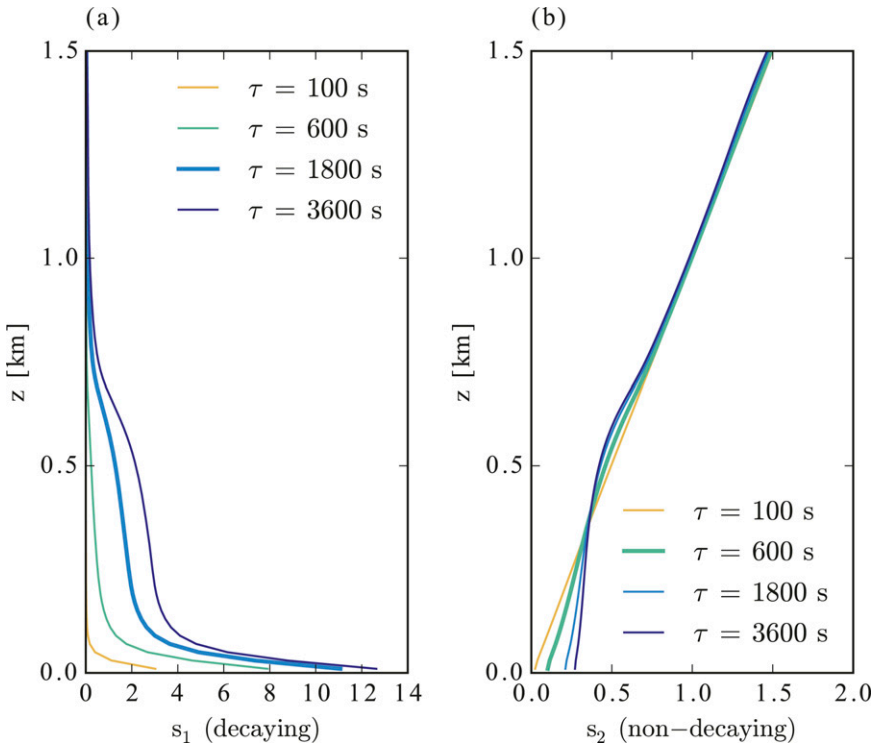


FIG. B1. Vertical profiles of slab-averaged (a) $s_1$ with different decay time scales and (b) $s_2$ with different relaxation time scales.

Instead of a cloud-resolving model, a denoised wavelet-based LES model could potentially be used to resolve subgrid moist convection in the wavelet domain instead of the spatial domain. Multiresolution methods have already been implemented in several engineering problems (Schneider and Vasilyev 2010; Okamoto et al. 2011b; De Stefano and Vasilyev 2013). Indeed, the coherent part of the flow represents only ~7% of the total wavelet coefficients of the full flow so that most of the transport can be represented with very few wavelet coefficients. In addition, the wavelet coefficients become sparser at small scales. In other words, improved convective parameterization representation could potentially be achieved with a compression algorithm that would represent and evaluate the evolution of the coherent flow only, which only represents a small fraction of the total field yet describes most of the transport. This wavelet-based extraction for parameterization will be evaluated in further studies.

## 4. Summary and conclusions

A new method, classifying updrafts, downdrafts/shells, (environmental) subsidence, and other flow structures in the LES-simulated boundary and cloud layers, has been introduced. Denoised parts of the vertical velocity, decaying passive scalar, and nondecaying passive scalar are obtained using the CVE filtering technique, and the coherent part is divided into eight flow structures based on the signs of perturbations of the three coherent variables. The method can, for the first time, evaluate the frequency and flux contribution of each of the different coherent structures both in the boundary layer and cloud layer. Updrafts and subsidence are the most frequent and dominant transporters of heat and moisture in the boundary layer. The two flow patterns with downdrafts/shells clearly show the detailed structure of horizontal convective rolls in the boundary layer. In the cloud layer, the frequency of ascendance is comparable to that of subsidence and its contribution to the vertical turbulent fluxes of heat and moisture balances that of subsidence. The downdraft/shell does not occur as frequently as subsidence, but it contributes significantly to the vertical transport of heat and moisture in both the boundary and cloud layers. The role of the downdraft/shell is distinct, especially in the upper cloud layer, where only it and updraft regions are significant transporters of heat and moisture.

The new classification method in this study extracts coherent structures in the unsaturated boundary layer

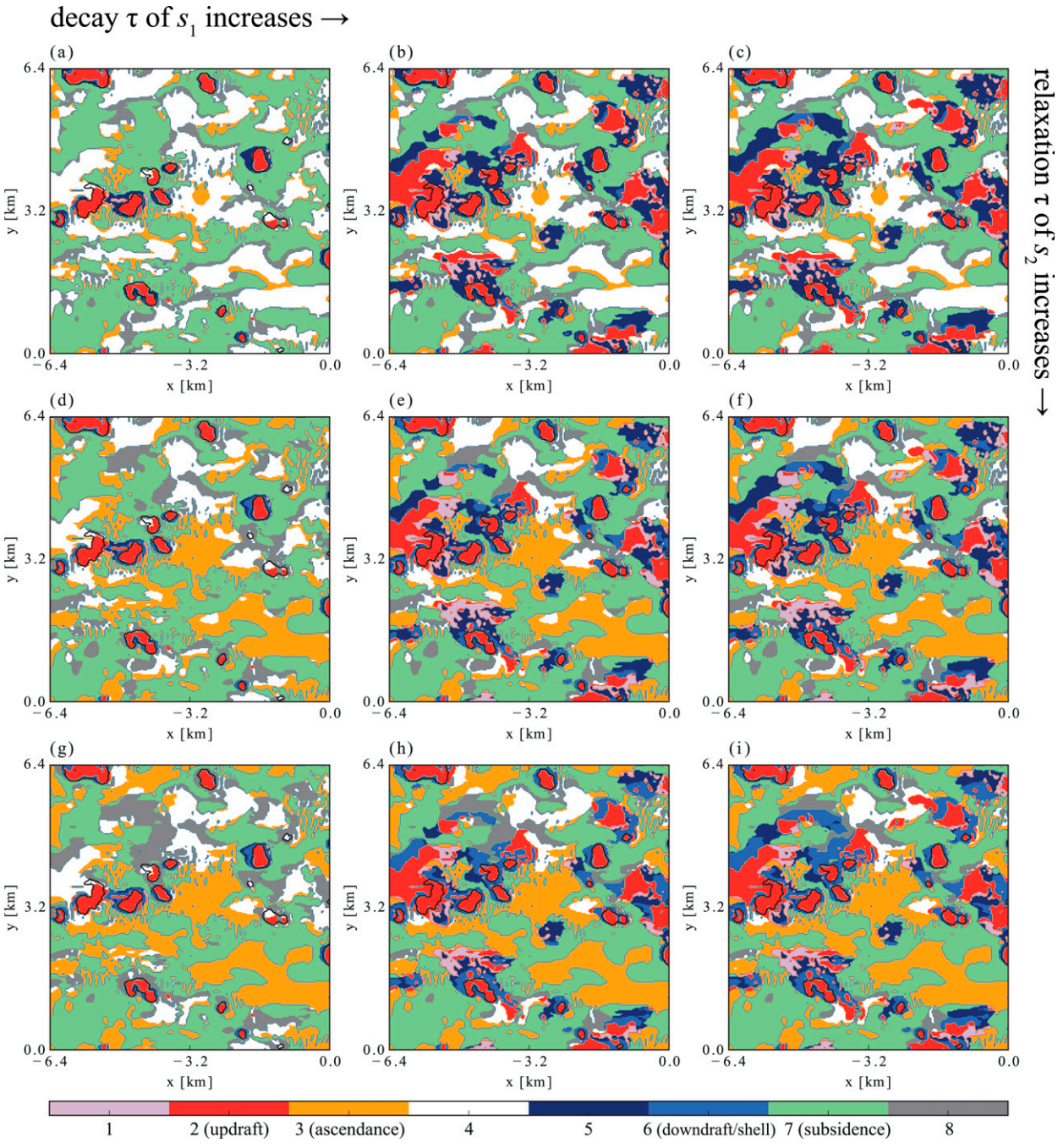


FIG. B2. Octant fields of $(w^c, s_1^c, s_2^c)$ at $t = 21\,600$ s and $z = 850$ m with (decay time scale, relaxation time scale) of (a) (100, 100), (b) (1800, 100), (c) (3600, 100), (d) (100, 600), (e) (1800, 600), (f) (3600, 600), (g) (100, 3600), (h) (1800, 3600), and (i) (3600, 3600) s. The contours of 0.01 g kg$^{-1}$ liquid water mixing ratio are added.

and cloud layer. This method is expected to help track continuous evolution of individual convective updrafts and their aggregation across the boundary between different atmospheric layers. With the help of tracking algorithm, this method can also help us understand the entrainment and detrainment of individual coherent structures. Further study focusing on the entrainment and detrainment of coherent structures in shallow and deep convections is being prepared.

It also should be stressed that the method efficiently tracks essential flow structures of shallow convection. Above the surface layer, less than 10% of wavelet

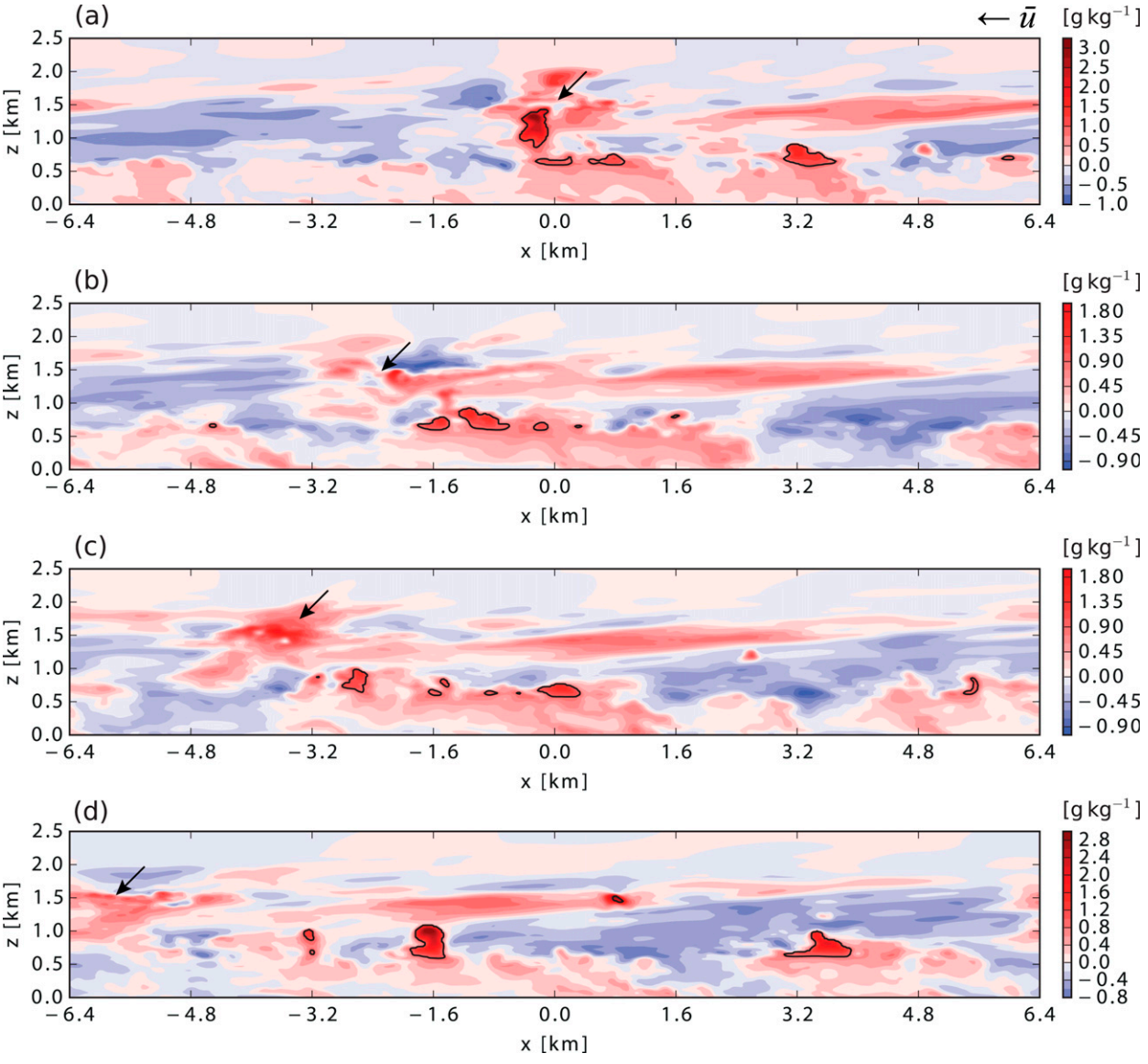


FIG. C1. Fields of perturbation of coherent total water mixing ratio in the $x$–$z$ plane at $y = 4412.5$ m at $t =$ (a) 20 880, (b) 21 120, (c) 21 360, and (d) 21 600 s. The contours of 0.01 g kg$^{-1}$ liquid water mixing ratio are added.

coefficients are used to reconstruct coherent structures that retain more than 95% of momentum transport in the vertical direction. In the future, adaptive wavelet discretizations could potentially be used for simulations, which benefit from the compression properties to reduce CPU and memory requirements of the computations.

*Acknowledgments.* The authors would like to acknowledge three anonymous reviewers for their valuable comments. This work was supported by NASA new investigator Grant NNX14AI36G, DOE Early Career Grant DE-SC0014203, and GoAmazon DE-SC0011094.

## APPENDIX A

### Octant Analysis of Nonfiltered LES Data

Octant analysis of nonfiltered $(w, s_1, s_2)$, that of $(w, s_1^c, s_2^c)$, and that of $(w^c, s_1, s_2)$ at $t = 21\,600$ s and $z = 350$, 850, and 1450 m are compared in Fig. A1. The octant fields of the filtered vertical velocity and the nonfiltered scalars in Figs. A1g–i are very similar to the octant fields of filtered variables in Fig. 8. CVE filtering of the two scalars slightly changes the results. In contrast, the octant fields of the nonfiltered vertical velocity and the filtered and nonfiltered scalars show small-scale

fluctuations between ascendance and subsidence and between fourth and eighth octants in the cloud layer (Figs. A1b,c,e,f). These small fluctuations are mainly due to the small-scale gravity waves, and they interrupt a clear identification of coherent structures in the environmental region.

## APPENDIX B

### Sensitivity to the Decay Time Scale of $s_1$ and Relaxation Time Scale of $s_2$

Four additional 1-h LES experiments, starting from the LES data at $t = 5$ h, are performed to check the sensitivity to the time scales of the two passive scalars. The initial (at $t = 5$ h) concentrations of the two scalars are set to zero and the linear profile, respectively, and both the time scales are set to 100, 600, 1800, and 3600 s in the four numerical experiments, respectively. Figure B1 shows the vertical profiles of slab-averaged decaying and nondecaying scalars, respectively. The concentration of decaying scalar decreases with decreasing decay time scale and that of nondecaying scalar relaxes more toward the initial profile with decreasing relaxation time scale. Thus, a short decay time scale helps us avoid oversaturation of the decaying scalar, and a short relaxation time scale enables maintaining a quasi-steady state of the nondecaying scalar.

Figure B2 shows the fields of octants at $z = 850$ m and $t = 21\,600$ s with several combinations of decay and relaxation time scales. As seen in Fig. B2, interchange between nearby octants (e.g., fifth and sixth octants) depending on time scales is inevitable. Despite the interchange, the change of flux contribution of individual octants is negligible (not shown) except for the shortest time scales because changeable parts are actually weak. Too-rapid decay (relaxation), however, suppresses weak but effective structures surrounding cloudy updrafts (Fig. B2a) and also change flux contribution of individual octants. Thus, we also avoid too-short decay and relaxation time scales.

## APPENDIX C

### Dissipating Structures of Moisture in the Upper Cloud Layer

Figure C1 shows a vertical cross sections in the $x$–$z$ plane (at $y = 4412.5$ m) of the perturbation of coherent total water mixing ratio at $t = 20\,880$, 21 120, 21 360, and 21 600 s. The 240-s spaced series of moisture perturbation fields illustrate dissipation of cloudy updrafts, for instance at $x = 0$ km and $z = 1$–1.5 km, and advection of dissipating structures following the mean wind (easterly in the cloud layer). Floating moisture in the upper cloud and inversion layers tends to decay slowly while moisture in the boundary layer is transported quickly through the strong cloudy updrafts (Figs. 6, 9, 10). After dissipation of the updrafts, detrained moisture remains in nonturbulent regions, being advected by the easterly mean wind (Figs. C1b–d). The elongated structures might be attributed to the vertical gradient of mean wind (weakening easterly with height) and the relatively long time scale of moisture dissipation in the nonturbulent regions. It is not clear that these kinds of structures can be directly related to the passive clouds in Stull (1988), and their role is unclear. However, the amount of moisture in the upper cloud and inversion layers must affect the condensation of newly uprising convections, and thus the dissipating flow structures deserve further study.

## REFERENCES


Abma, D., T. Heus, and J. P. Mellado, 2013: Direct numerical simulation of evaporative cooling at the lateral boundary of shallow cumulus clouds. *J. Atmos. Sci.*, **70**, 2088–2102, doi:10.1175/JAS-D-12-0230.1.

Arakawa, A., J.-H. Jung, and C.-M. Wu, 2011: Toward unification of the multiscale modeling of the atmosphere. *Atmos. Chem. Phys.*, **11**, 3731–3742, doi:10.5194/acp-11-3731-2011.

Bechtold, P., M. Köhler, T. Jung, F. Doblas-Reyes, M. Leutbecher, M. J. Rodwell, F. Vitart, and G. Balsamo, 2008: Advances in simulating atmospheric variability with the ECMWF model: From synoptic to decadal time-scales. *Quart. J. Roy. Meteor. Soc.*, **134**, 1337–1351, doi:10.1002/qj.289.

Beron-Vera, F. J., M. J. Olascoaga, G. Haller, M. Farazmand, J. Trinanes, and Y. Wang, 2015: Dissipative inertial transport patterns near coherent Lagrangian eddies in the ocean. *Chaos*, **25**, 087412, doi:10.1063/1.4928693.

Betts, A. K., 1985: Mixing line analysis of clouds and cloudy boundary layers. *J. Atmos. Sci.*, **42**, 2751–2763, doi:10.1175/1520-0469(1985)042<2751:MLAOCA>2.0.CO;2.

Bjerkness, J., 1938: Saturated-adiabatic ascent of air through dry-adiabatically descending environment. *Quart. J. Roy. Meteor. Soc.*, **64**, 325–330.

Bony, S., and Coauthors, 2006: How well do we understand and evaluate climate change feedback processes? *J. Climate*, **19**, 3445–3482, doi:10.1175/JCLI3819.1.

Bos, W. J. T., S. Futatani, S. Benkadda, M. Farge, and K. Schneider, 2008: The role of coherent vorticity in turbulent transport in resistive drift-wave turbulence. *Phys. Plasmas*, **15**, 072305, doi:10.1063/1.2956640.

Bretherton, C. S., 1987: A theory for nonprecipitating moist convection between two parallel plates. Part I: Thermodynamics and "linear" solutions. *J. Atmos. Sci.*, **44**, 1809–1827, doi:10.1175/1520-0469(1987)044<1809:ATFNMC>2.0.CO;2.

——, and P. K. Smolarkiewicz, 1989: Gravity waves, compensating subsidence and detrainment around cumulus clouds. *J. Atmos. Sci.*, **46**, 740–759, doi:10.1175/1520-0469(1989)046<0740:GWCSAD>2.0.CO;2.

Brown, A. R., and Coauthors, 2002: Large-eddy simulation of the diurnal cycle of shallow cumulus convection over land.

*Quart. J. Roy. Meteor. Soc.*, **128**, 1075–1093, doi:10.1256/003590002320373210.

Couvreux, F., F. Hourdin, and C. Rio, 2010: Resolved versus parametrized boundary-layer plumes. Part I: A parametrization-oriented conditional sampling in large-eddy simulations. *Bound.-Layer Meteor.*, **134**, 441–458, doi:10.1007/s10546-009-9456-5.

D'Andrea, F., P. Gentine, A. K. Betts, and B. R. Lintner, 2014: Triggering deep convection with a probabilistic plume model. *J. Atmos. Sci.*, **71**, 3881–3901, doi:10.1175/JAS-D-13-0340.1.

Dawe, J. T., and P. H. Austin, 2011: The influence of the cloud shell on tracer budget measurements of LES cloud entrainment. *J. Atmos. Sci.*, **68**, 2909–2920, doi:10.1175/2011JAS3658.1.

de Rooy, W. C., and Coauthors, 2013: Entrainment and detrainment in cumulus convection: An overview. *Quart. J. Roy. Meteor. Soc.*, **139**, 1–19, doi:10.1002/qj.1959.

De Stefano, G., and O. V. Vasilyev, 2013: Wavelet-based adaptive large-eddy simulation with explicit filtering. *J. Comput. Phys.*, **238**, 240–254, doi:10.1016/j.jcp.2012.09.030.

Donoho, D. L., and J. M. Johnstone, 1994: Ideal spatial adaptation by wavelet shrinkage. *Biometrika*, **81**, 425–455, doi:10.1093/biomet/81.3.425.

Dryden, H. L., 1948: Recent advances in the mechanics of boundary layer flow. *Adv. Appl. Mech.*, **1**, 1–40, doi:10.1016/S0065-2156(08)70097-8.

Farge, M., K. Schneider, and N. Kevlahan, 1999: Non-Gaussianity and coherent vortex simulation for two-dimensional turbulence using an adaptive orthogonal wavelet basis. *Phys. Fluids*, **11**, 2187, doi:10.1063/1.870080.

——, G. Pellegrino, and K. Schneider, 2001: Coherent vortex extraction in 3D turbulent flows using orthogonal wavelets. *Phys. Rev. Lett.*, **87**, 054501, doi:10.1103/PhysRevLett.87.054501.

——, K. Schneider, G. Pellegrino, A. A. Wray, and R. S. Rogallo, 2003: Coherent vortex extraction in three-dimensional homogeneous turbulence: Comparison between CVS-wavelet and POD-Fourier decompositions. *Phys. Fluids*, **15**, 2886–2898, doi:10.1063/1.1599857.

——, ——, and P. Devynck, 2006: Extraction of coherent bursts from turbulent edge plasma in magnetic fusion devices using orthogonal wavelets. *Phys. Plasmas*, **13**, 042304, doi:10.1063/1.2172350.

Finnigan, J. J., R. H. Shaw, and E. G. Patton, 2009: Turbulence structure above a vegetation canopy. *J. Fluid Mech.*, **637**, 387–424, doi:10.1017/S0022112009990589.

Foster, R. C., F. Vianey, P. Drobinski, and P. Carlotti, 2006: Near-surface coherent structures and the vertical momentum flux in a large-eddy simulation of the neutrally-stratified boundary layer. *Bound.-Layer Meteor.*, **120**, 229–255, doi:10.1007/s10546-006-9054-8.

Gentine, P., A. K. Betts, B. R. Lintner, K. L. Findell, C. C. van Heerwaarden, A. Tzella, and F. D'Andrea, 2013a: A probabilistic bulk model of coupled mixed layer and convection. Part I: Clear-sky case. *J. Atmos. Sci.*, **70**, 1543–1556, doi:10.1175/JAS-D-12-0145.1.

——, ——, ——, ——, ——, and F. D'Andrea, 2013b: A probabilistic bulk model of coupled mixed layer and convection. Part II: Shallow convection case. *J. Atmos. Sci.*, **70**, 1557–1576, doi:10.1175/JAS-D-12-0146.1.

Gheisi, A. R., M. R. Alavimoghaddam, and A. Dadrasmoghaddam, 2006: Markovian–Octant analysis based stable turbulent shear stresses in near-bed bursting phenomena of vortex settling chamber. *Environ. Fluid Mech.*, **6**, 549–572, doi:10.1007/s10652-006-9009-0.

Glenn, I. B., and S. K. Krueger, 2014: Downdrafts in the near cloud environment of deep convective updrafts. *J. Adv. Model. Earth Syst.*, **6**, 1–8, doi:10.1002/2013MS000261.

Gregory, D., 2001: Estimation of entrainment rate in simple models of convective clouds. *Quart. J. Roy. Meteor. Soc.*, **127**, 53–72, doi:10.1002/qj.49712757104.

Guingo, M., and J.-P. Minier, 2008: A stochastic model of coherent structures for particle deposition in turbulent flows. *Phys. Fluids*, **20**, 053303, doi:10.1063/1.2908934.

Haller, G., and G. Yuan, 2000: Lagrangian coherent structures and mixing in two-dimensional turbulence. *Physica D*, **147**, 352–370, doi:10.1016/S0167-2789(00)00142-1.

Heus, T., and H. J. J. Jonker, 2008: Subsiding shells around shallow cumulus clouds. *J. Atmos. Sci.*, **65**, 1003–1018, doi:10.1175/2007JAS2322.1.

——, G. van Dijk, H. J. J. Jonker, and H. E. A. Van den Akker, 2008: Mixing in shallow cumulus clouds studied by Lagrangian particle tracking. *J. Atmos. Sci.*, **65**, 2581–2597, doi:10.1175/2008JAS2572.1.

Hill, M. J. M., 1894: On a spherical vortex. *Philos. Trans. Roy. Soc.*, **A185**, 213–245, doi:10.1098/rsta.1894.0006.

Holland, J. Z., and E. M. Rasmusson, 1973: Measurement of the atmospheric mass, energy, and momentum budgets over a 500-kilometer square of tropical ocean. *Mon. Wea. Rev.*, **101**, 44–57, doi:10.1175/1520-0493(1973)101<0044:MOTAME>2.3.CO;2.

Jonker, H. J. J., T. Heus, and P. P. Sullivan, 2008: A refined view of vertical mass transport by cumulus convection. *Geophys. Res. Lett.*, **35**, L07810, doi:10.1029/2007GL032606.

Kadoch, B., K. Iyer, D. Donzis, K. Schneider, M. Farge, and P. K. Yeung, 2011: On the role of vortical structures for turbulent mixing using direct numerical simulation and wavelet-based coherent vorticity extraction. *J. Turbul.*, **12**, 1–17, doi:10.1080/14685248.2011.562511.

Katul, G., G. Kuhn, J. Schieldge, and C.-I. Hsieh, 1997: The ejection-sweep character of scalar fluxes in the unstable surface layer. *Bound.-Layer Meteor.*, **83**, 1–26, doi:10.1023/A:1000293516830.

——, D. Poggi, D. Cava, and J. Finnigan, 2006: The relative importance of ejections and sweeps to momentum transfer in the atmospheric boundary layer. *Bound.-Layer Meteor.*, **120**, 367–375, doi:10.1007/s10546-006-9064-6.

Kershaw, R., 1995: Parametrization of momentum transport by convectively generated gravity waves. *Quart. J. Roy. Meteor. Soc.*, **121**, 1023–1040, doi:10.1002/qj.49712152505.

Khairoutdinov, M. F., and D. A. Randall, 2001: A cloud resolving model as a cloud parameterization in the NCAR Community Climate System Model: Preliminary results. *Geophys. Res. Lett.*, **28**, 3617–3620, doi:10.1029/2001GL013552.

——, ——, and C. DeMott, 2005: Simulations of the atmospheric general circulation using a cloud-resolving model as a superparameterization of physical processes. *J. Atmos. Sci.*, **62**, 2136–2154, doi:10.1175/JAS3453.1.

Khujadze, G., R. N. van Yen, K. Schneider, M. Oberlack, and M. Farge, 2011: Coherent vorticity extraction in turbulent boundary layers using orthogonal wavelets. *J. Phys. Conf. Ser.*, **318**, 022011, doi:10.1088/1742-6596/318/2/022011.

Kim, D., A. H. Sobel, A. D. Del Genio, Y. Chen, S. J. Camargo, M. S. Yao, M. Kelley, and L. Nazarenko, 2012: The tropical subseasonal variability simulated in the NASA GISS general circulation model. *J. Climate*, **25**, 4641–4659, doi:10.1175/JCLI-D-11-00447.1.

Kim, S., and S. Park, 2003: Coherent structures near the surface in a strongly sheared convective boundary layer generated by

large-eddy simulation. *Bound.-Layer Meteor.*, **106**, 35–60, doi:10.1023/A:1020811015189.

Kuang, Z., and C. S. Bretherton, 2006: A mass-flux scheme view of a high-resolution simulation of a transition from shallow to deep cumulus convection. *J. Atmos. Sci.*, **63**, 1895–1909, doi:10.1175/JAS3723.1.

LeMone, M. A., 1973: The structure and dynamics of horizontal roll vortices in the planetary boundary layer. *J. Atmos. Sci.*, **30**, 1077–1091, doi:10.1175/1520-0469(1973)030<1077:TSADOH>2.0.CO;2.

Li, D., and E. Bou-Zeid, 2011: Coherent structures and the dissimilarity of turbulent transport of momentum and scalars in the unstable atmospheric surface layer. *Bound.-Layer Meteor.*, **140**, 243–262, doi:10.1007/s10546-011-9613-5.

Li, F., D. Rosa, W. D. Collins, and M. F. Wehner, 2012: ''Super-parameterization'': A better way to simulate regional extreme precipitation. *J. Adv. Model. Earth Syst.*, **4**, M04002, doi:10.1029/2011MS000106.

Lin, C.-L., 1999: Near-grid-scale energy transfer and coherent structures in the convective planetary boundary layer. *Phys. Fluids*, **11**, 3482, doi:10.1063/1.870206.

McNaughton, K. G., and Y. Brunet, 2002: Townsend's hypothesis, coherent structures and Monin–Obukhov similarity. *Bound.-Layer Meteor.*, **102**, 161–175, doi:10.1023/A:1013171312407.

Moeng, C.-H., and P. P. Sullivan, 1994: A comparison of shear- and buoyancy-driven planetary boundary layer flows. *J. Atmos. Sci.*, **51**, 999–1022, doi:10.1175/1520-0469(1994)051<0999:ACOSAB>2.0.CO;2.

Mrowiec, A. A., O. M. Pauluis, A. M. Fridlind, and A. S. Ackerman, 2015: Properties of a mesoscale convective system in the context of an isentropic analysis. *J. Atmos. Sci.*, **72**, 1945–1962, doi:10.1175/JAS-D-14-0139.1.

Neggers, R. J., 2009: A dual mass flux framework for boundary layer convection. Part II: Clouds. *J. Atmos. Sci.*, **66**, 1489–1506, doi:10.1175/2008JAS2636.1.

Okamoto, N., K. Yoshimatsu, K. Schneider, M. Farge, and Y. Kaneda, 2007: Coherent vortices in high resolution direct numerical simulation of homogeneous isotropic turbulence: A wavelet viewpoint. *Phys. Fluids*, **19**, 115109, doi:10.1063/1.2771661.

——, ——, ——, and ——, 2011a: Intermittency of quasi-static magnetohydrodynamic turbulence: A wavelet viewpoint. *J. Phys. Conf. Ser.*, **318**, 072035, doi:10.1088/1742-6596/318/7/072035.

——, ——, ——, ——, and Y. Kaneda, 2011b: Coherent vorticity simulation of three-dimensional forced homogeneous isotropic turbulence. *Multiscale Model. Simul.*, **9**, 1144–1161, doi:10.1137/10079598X.

Pauluis, O. M., and A. A. Mrowiec, 2013: Isentropic analysis of convective motions. *J. Atmos. Sci.*, **70**, 3673–3688, doi:10.1175/JAS-D-12-0205.1.

Raupach, M. R., 1981: Conditional statistics of Reynolds stress in rough-wall and smooth-wall turbulent boundary layers. *J. Fluid Mech.*, **108**, 363–382, doi:10.1017/S0022112081002164.

Richter, D. H., and P. P. Sullivan, 2014: Modification of near-wall coherent structures by inertial particles. *Phys. Fluids*, **26**, 103304, doi:10.1063/1.4900583.

Rio, C., and F. Hourdin, 2008: A thermal plume model for the convective boundary layer: Representation of cumulus clouds. *J. Atmos. Sci.*, **65**, 407–425, doi:10.1175/2007JAS2256.1.

——, ——, F. Couvreux, and A. Jam, 2010: Resolved versus parametrized boundary-layer plumes. Part II: Continuous formulations of mixing rates for mass-flux schemes. *Bound.-Layer Meteor.*, **135**, 469–483, doi:10.1007/s10546-010-9478-z.

Robinson, S., 1991: Coherent motions in the turbulent boundary layer. *Annu. Rev. Fluid Mech.*, **23**, 601–639, doi:10.1146/annurev.fl.23.010191.003125.

Romps, D. M., 2010: A direct measure of entrainment. *J. Atmos. Sci.*, **67**, 1908–1927, doi:10.1175/2010JAS3371.1.

Santanello, J. A., C. D. Peters-Lidard, S. V. Kumar, C. Alonge, and W.-K. Tao, 2009: A modeling and observational framework for diagnosing local land–atmosphere coupling on diurnal time scales. *J. Hydrometeor.*, **10**, 577–599, doi:10.1175/2009JHM1066.1.

——, ——, and ——, 2011: Diagnosing the sensitivity of local land–atmosphere coupling via the soil moisture–boundary layer interaction. *J. Hydrometeor.*, **12**, 766–786, doi:10.1175/JHM-D-10-05014.1.

Schneider, K., and O. V. Vasilyev, 2010: Wavelet methods in computational fluid dynamics. *Annu. Rev. Fluid Mech.*, **42**, 473–503, doi:10.1146/annurev-fluid-121108-145637.

——, M. Farge, G. Pellegrino, and M. M. Rogers, 2005: Coherent vortex simulation of three-dimensional turbulent mixing layers using orthogonal wavelets. *J. Fluid Mech.*, **534**, 39–66, doi:10.1017/S0022112005004234.

Sherwood, S. C., D. Hernández-Deckers, M. Colin, and F. Robinson, 2013: Slippery thermals and the cumulus entrainment paradox. *J. Atmos. Sci.*, **70**, 2426–2442, doi:10.1175/JAS-D-12-0220.1.

Siebesma, A. P., and J. W. M. Cuijpers, 1995: Evaluation of parametric assumptions for shallow cumulus convection. *J. Atmos. Sci.*, **52**, 650–666, doi:10.1175/1520-0469(1995)052<0650:EOPAFS>2.0.CO;2.

——, and Coauthors, 2003: A large eddy simulation intercomparison study of shallow cumulus convection. *J. Atmos. Sci.*, **60**, 1201–1219, doi:10.1175/1520-0469(2003)60<1201:ALESIS>2.0.CO;2.

——, P. M. M. Soares, and J. Teixeira, 2007: A combined eddy-diffusivity mass-flux approach for the convective boundary layer. *J. Atmos. Sci.*, **64**, 1230–1248, doi:10.1175/JAS3888.1.

Soares, P. M. M., P. M. A. Miranda, P. Siebesma, and J. Teixeira, 2004: An eddy-diffusivity/mass-flux parametrization for dry and shallow cumulus convection. *Quart. J. Roy. Meteor. Soc.*, **130**, 3365–3383, doi:10.1256/qj.03.223.

Stevens, B., and A. Seifert, 2008: Understanding macrophysical outcomes of microphysical choices in simulations of shallow cumulus convection. *J. Meteor. Soc. Japan*, **86A**, 143–162, doi:10.2151/jmsj.86A.143.

——, C.-H. Moeng, and P. P. Sullivan, 1999: Large-eddy simulations of radiatively driven convection: Sensitivities to the representation of small scales. *J. Atmos. Sci.*, **56**, 3963–3984, doi:10.1175/1520-0469(1999)056<3963:LESORD>2.0.CO;2.

——, and Coauthors, 2005: Evaluation of large-eddy simulations via observations of nocturnal marine stratocumulus. *Mon. Wea. Rev.*, **133**, 1443–1462, doi:10.1175/MWR2930.1.

Stull, R. B., 1988: *An Introduction to Boundary Layer Meteorology*. Kluwer Academic, 666 pp.

Sullivan, P. P., C.-H. Moeng, B. Stevens, D. H. Lenschow, and S. D. Mayor, 1998: Structure of the entrainment zone capping the convective atmospheric boundary layer. *J. Atmos. Sci.*, **55**, 3042–3064, doi:10.1175/1520-0469(1998)055<3042:SOTEZC>2.0.CO;2.

Sušelj, K., J. Teixeira, and D. Chung, 2013: A unified model for moist convective boundary layers based on a stochastic eddy-diffusivity/mass-flux parameterization. *J. Atmos. Sci.*, **70**, 1929–1953, doi:10.1175/JAS-D-12-0106.1.

Tiedtke, M., 1989: A comprehensive mass flux scheme for cumulus parameterization in large-scale models. *Mon. Wea.*

*Rev.*, **117**, 1779–1800, doi:10.1175/1520-0493(1989)117<1779:ACMFSF>2.0.CO;2.

Volino, R. J., and T. W. Simon, 1994: An application of octant analysis to turbulent and transitional flow data. *J. Turbomach.*, **116**, 752–758, doi:10.1115/1.2929469.

Wallace, J. M., 2016: Quadrant analysis in turbulence research: History and evolution. *Annu. Rev. Fluid Mech.*, **48**, 131–158, doi:10.1146/annurev-fluid-122414-034550.

Watanabe, T., 2004: Large-eddy simulation of coherent turbulence structures associated with scalar ramps over plant canopies. *Bound.-Layer Meteor.*, **112**, 307–341, doi:10.1023/B:BOUN.0000027912.84492.54.

Wilczek, M., B. Kadoch, K. Schneider, R. Friedrich, and M. Farge, 2012: Conditional vorticity budget of coherent and incoherent flow contributions in fully developed homogeneous isotropic turbulence. *Phys. Fluids*, **24**, 035108, doi:10.1063/1.3694807.

Yano, J.-I., P. Bechtold, J.-L. Redelsperger, and F. Guichard, 2004: Wavelet-compressed representation of deep moist convection. *Mon. Wea. Rev.*, **132**, 1472–1486, doi:10.1175/1520-0493(2004)132<1472:WRODMC>2.0.CO;2.

Zeri, M., and L. D. de Abreu Sá, 2011: Scale dependence of coherent structures' contribution to the daytime buoyancy heat flux over the Pantanal wetland, Brazil. *Atmos. Sci. Lett.*, **12**, 200–206, doi:10.1002/asl.311.